Airborne observations of peroxy radicals during the EMeRGe campaign in Europe

[1][+]Midhun George, [1]Maria Dolores Andrés Hernández, [1*]Vladyslav Nenakhov, [1]Yangzhuoran Liu, [1]John Philip Burrows; [2]Birger Bohn; [3]Eric Förster, [3]Florian Obersteiner, [3]Andreas Zahn; [4]Theresa Harlaß, [4]Helmut Ziereis, [4]Hans Schlager; [5]Benjamin Schreiner, [5]Flora Kluge, [5]Katja Bigge, and [5]Klaus Pfeilsticker

[1] Institute of Environmental Physics, University of Bremen, Germany
[2] Institute of Energy and Climate Research, IEK-8: Troposphere, Forschungszentrum Jülich GmbH, Jülich, Germany
[3] Institute of Meteorology and Climate Research, Karlsruhe Institute of Technology, Karlsruhe, Germany
[4] Deutsches Zentrum für Luft- und Raumfahrt (DLR), Institut für Physik der Atmosphäre, Oberpfaffenhofen, Germany
[5] Institute of Environmental Physics, University of Heidelberg, Heidelberg, Germany
[+] now at University of Leeds, Leeds, United Kingdom
[*] now at Flight Experiments, DLR Oberpfaffenhoffen, Germany

Correspondence to M. George (M.George@leeds.ac.uk) and M. D. Andrés Hernández (lola@iup.physik.uni-bremen.de).

Abstract. In this study, airborne measurements of the sum of hydroperoxyl (HO_2) and organic peroxy (RO_2) radicals that react with nitrogen monoxide (NO) to produce nitrogen dioxide, (NO_2), coupled with actinometry and other key trace gases measurements, have been used to test the current understanding of the fast photochemistry in the outflow of major population centres. The measurements were made during the airborne campaign of the EMeRGe (**E**ffect of **M**egacities on the transport and transformation of pollutants on the **R**egional to **G**lobal scal**e**s) project in Europe on-board the **H**igh **A**ltitude **Lo**ng range research aircraft (HALO). The measurements of RO_2^* on HALO were made using the in-situ instrument **P**eroxy **R**adical **C**hemical **E**nhancement and **A**bsorption **S**pectrometer (PeRCEAS). RO_2^* is to a good approximation the sum of peroxy radicals reacting with NO to produce NO_2. RO_2^* mixing ratios up to 120 pptv were observed in air masses of different origins and composition under different local actinometrical conditions during seven HALO research flights in July 2017 over Europe.

Radical production rates were estimated using knowledge of the photolysis frequencies and the RO_2^* precursor concentrations measured on-board, as well as the relevant rate coefficients. Generally, high RO_2^* concentrations were measured in air masses with high production rates. In the airmasses investigated RO_2^* is primarily produced by the reaction of O^1D with water vapour, and the photolysis of nitrous acid (HONO) and of the oxygenated volatile organic compounds (OVOC, e.g., formaldehyde (HCHO), and glyoxal (CHOCHO)). Due to their short lifetime in most environments, the RO_2^* concentrations are expected to be in a photostationary steady state (PSS), i.e., it is assumed a balance between production and loss rates. The RO_2^* production and loss rates and the suitability of PSS assumptions to estimate the RO_2^* mixing ratios and variability during the airborne observations are discussed. The PSS assumption for RO_2^* is considered robust enough to calculate RO_2^* mixing ratios for most conditions encountered in the air masses measured. The similarities and discrepancies between measured and PSS calculated RO_2^* mixing ratios are discussed. The dominant terminating processes for RO_2^* in the pollution plumes measured up to 2000 m are the formation of nitrous acid, nitric acid and organic nitrates. Above 2000 m, $HO_2 – HO_2$ and $HO_2 – RO_2$ reactions dominate the RO_2^* removal. RO_2^* calculations by the PSS analytical expression inside the pollution plumes probed often underestimated the measurements. The underestimation is attributed to the limitations of the PSS equation used for the analysis. In particular, this expression does not account for the yields of RO_2^* from the oxidation and photolysis of volatile organic compounds, VOCs, and OVOCs other than those measured during the EMeRGe research flights in Europe. In air masses with NO mixing ratios ≤ 50 pptv and low VOC/NO ratios, the overestimation of the RO_2^* measured observed may be caused by the formation of H_2O and O_2 from OH and HO_2, being about 4 times faster than the rate of the OH oxidation reaction of the dominant OVOCs considered.

1. Introduction

Hydroperoxyl (HO_2) and organic peroxy (RO_2, where R stands for any organic group) radicals are reactive species that play a key role in the chemistry of the troposphere. In combination with the hydroxyl (OH) radical, HO_2 and RO_2 take part in rapid chemical processes that control the lifetime of many key trace constituents in the troposphere. Examples of key tropospheric processes involving HO_2 and RO_2 are as follows:

- the catalytic cycles which produce and destroy ozone (O_3)
- the generation of inorganic acids, which are precursors of aerosol (e.g., sulphuric acid, H_2SO_4) and important chemical constituents (e.g., nitric acid, HNO_3) in both summer and winter smog
- the generation of organic acids; the production of hygroscopic hydrogen peroxide (H_2O_2) and organic peroxides (ROOH), which enter aerosol and cloud droplets
- the generation of organic peroxy nitrates (RO_2NO_2), peroxyacetyl nitrate ($CH_3COO_2NO_2$, PAN) and other summer smog constituents.

The abundance of HO_2 and RO_2 in the free troposphere has a non-linear and complex dependency on photochemistry, initiated by solar actinic radiation, and on the concentration of the precursors, such as carbon monoxide (CO), **v**olatile **o**rganic **c**ompounds (VOCs), and peroxides. It also strongly depends on the amounts of nitrogen monoxide (NO) and nitrogen dioxide (NO_2) due to the gas-phase reactions of NO and NO_2 with the OH and organic oxy (RO) radicals formed during the radical interconversion. The main production and loss processes of HO_2 and RO_2 in the troposphere are summarised as follows:

a) Production processes of HO_2 and RO_2

$$O_3 + h\nu \ (\lambda < 320 \text{ nm}) \rightarrow O(^1D) + O_2 \tag{R1}$$

$$O(^1D) + H_2O \rightarrow 2OH \tag{R2a}$$

$$O(^1D) + N_2 \rightarrow O(^3P) + N_2 \tag{R2b}$$

$$O(^1D) + O_2 \rightarrow O(^3P) + O_2 \tag{R2c}$$

$$HONO + h\nu \ (\lambda \leq 400 \text{ nm}) \rightarrow OH + NO \tag{R3}$$

$$H_2O_2 + h\nu \rightarrow 2OH \tag{R4}$$

$$OH + O_3 \rightarrow HO_2 + O_2 \tag{R5}$$

$$OH + CO + O_2 \rightarrow HO_2 + CO_2 \tag{R6}$$

$$(*) \ OH + CH_4 + O_2 \rightarrow CH_3O_2 + H_2O \tag{R7}$$

$$(**) \ HCHO + h\nu \ (\lambda < 340 \text{ nm}) + 2O_2 \rightarrow 2HO_2 + CO \tag{R8}$$

$$(*)(**) \ CH_3CHO + h\nu \ (\lambda < 340 \text{ nm}) + 2O_2 \rightarrow CH_3O_2 + HO_2 + CO \tag{R9}$$
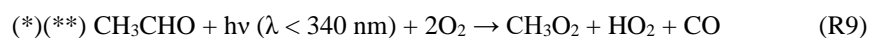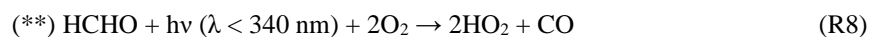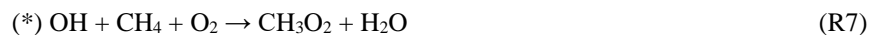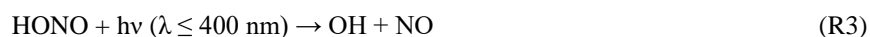
(*) The CH_3 produced from the oxidation of CH_4 or the photolysis of VOCs further reacts with O_2 to form CH_3O_2. The net or overall reaction is used because the formation of CH_3O_2 is much faster than the CH_3 formation due to the high amount of O_2 present in the atmosphere.
(**) H and CHO formed through the VOC photolysis further react with O_2 to form HO_2. The net reaction is used, because the formation of HO_2 is much faster than the H and CHO formation due to the high amount of O_2 present in the atmosphere.

(**) $CH_3C(O)CH_3 + h\nu$ ($\lambda < 340$ nm) $+ 2O_2 \rightarrow 2\,CH_3O_2 + CO$ (R10)

(**) $CHOCHO + h\nu + 2O_2 \xrightarrow{M} 2HO_2 + 2CO$ (R11)

75    $VOCs + OH \rightarrow OH + HO_2 + RO_2$ and other oxidation products   (R12)

alkenes $+ O_3 \rightarrow OH + RO_2 +$ other oxidation products   (R13)

  b) Loss processes of HO_2 and RO_2

$HO_2 + HO_2 \rightarrow H_2O_2 + O_2$ (R14)

80    $HO_2 + RO_2 \rightarrow ROOH + O_2$ (R15)

$RO_2 + RO_2 \rightarrow ROOH + R_{C-1}CHO + O_2$ (R16a)

$OH + HO_2 \rightarrow H_2O + O_2$ (R17)

$OH + OH \xrightarrow{M} H_2O_2$ (R18)

$OH + NO \xrightarrow{M} HONO$ (R19)

85    $OH + NO_2 \xrightarrow{M} HNO_3$ (R20)

$OH + HONO \rightarrow H_2O + NO_2$ (R21)
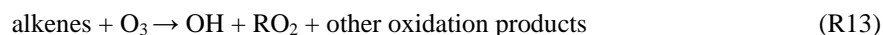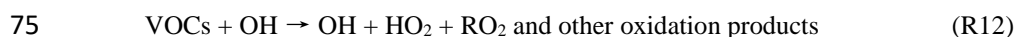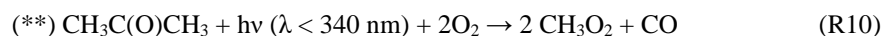
$RO + NO \xrightarrow{M} RONO$ (R22)

In addition, HO_2 and RO_2 participate in radical interconversion reactions such as:

$RO_2 + RO_2 \rightarrow RO + RO + O_2$ (R16b)

90    $HO_2 + NO \rightarrow OH + NO_2$ (R23)

$HO_2 + O_3 \rightarrow OH + 2O_2$ (R24)

$RO_2 + NO \rightarrow RO + NO_2$ (R25a)

$RO_2 + NO \rightarrow RONO_2$ (R25b)

$RO + O_2 \rightarrow R_{H-1}O + HO_2$ (R26)
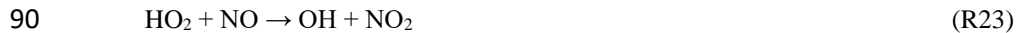
95   Reactions R23 and R25a are two of the most important reactions in the troposphere as they lead to O_3 formation via the reactions R27 and R28. The rate of the reaction R22 in the atmosphere compared to that of reaction R26 is negligible.

(**) H and CHO formed through the VOC photolysis further react with O_2 to form HO_2. The net reaction is used, because the formation of HO_2 is much faster than the H and CHO formation due to the high amount of O_2 present in the atmosphere.

100   The sum of HO_2 and RO_2 that react with NO to produce NO_2 can be estimated by assuming that the interconversion of NO to NO_2 reaches a **p**hotostationary **s**teady-**s**tate (PSS), in which production and loss of NO_2 are to a good approximation equal.

The PSS assumption for $[NO_2]$ in the following mechanism (reactions R23 to R29) leads to Eq. 1

$$HO_2 + NO \rightarrow OH + NO_2 \qquad\qquad\qquad\qquad\qquad\qquad (R23)$$

$$RO_2 + NO + O_2 \rightarrow R_{H-1}O + NO_2 + HO_2 \qquad\qquad\qquad (R25a + R26)$$

105     $$NO_2 + h\nu \ (\lambda < 400 \ nm) \rightarrow NO + O \qquad\qquad\qquad\qquad (R27)$$

$$O + O_2 \xrightarrow{M} O_3 \qquad\qquad\qquad\qquad\qquad\qquad\qquad\qquad (R28)$$

$$NO + O_3 \rightarrow NO_2 + O_2 \qquad\qquad\qquad\qquad\qquad\qquad\qquad (R29)$$

$$[HO_2 + RO_2]_{PSS} = \frac{k_{NO+O_3}}{k_{NO+(HO_2+RO_2)}} \left(\frac{j_{NO_2}[NO_2]}{k_{NO+O_3}[NO]} - [O_3] \right) \qquad\qquad (Eq.1)$$

where j_{NO_2} is the photolysis frequency of NO_2; k_{NO+O_3} (1.9×10^{-14} cm^3 molecules^{-1} s^{-1} at 298K and 1 atm.) is the rate coefficient

110   of the reaction of NO with O_3 and $k_{NO+(HO_2+RO_2)}$ is usually estimated for the most abundant peroxy radicals HO_2 and CH_3O_2 by assuming a 1:1 HO_2 to CH_3O_2 ratio and averaging the k_{NO+HO_2} (8.2×10^{-12} cm^3 molecules^{-1} s^{-1} at 298K and 1 atm.) and $k_{NO+CH_3O_2}$ (7.7×10^{-12} cm^3 molecules^{-1} s^{-1} at 298K and 1 atm.) rate coefficients for the reaction with NO. As noted by Parrish et al. (1986), the PSS assumption for NO_2 requires conditions with sufficient and stable solar irradiation, ensuring stable NO_2 photolysis rates (j_{NO_2}).

The radical calculation made on the assumption of the NO_2 steady state is very sensitive to the accuracy of the NO_2 to NO ratio

115   and the O_3 measurements. The comparison of $[HO_2 + RO_2]_{PSS}$ calculated using Eq.1 with ground-based (e.g., Ridley et al., 1992; Cantrell et al., 1997; Carpenter et al., 1998; Volz-Thomas et al., 2003), and airborne measurements, has shown in the past different degrees of agreement. The underestimations and overestimations found in air masses with different chemical compositions are not well understood. For the case of airborne measurements, the NO_2 steady state calculation generally overestimates the measured peroxy radicals (Cantrell et al., 2003a, 2003b). The differences observed could not be attributed to systematic changes in NO,

120   altitude, water vapour and temperature, although these variables are often correlated. The NO to NO_2 ratio calculated from NO measured using in-situ technique and NO_2 measured using remote sensing (more detail about the measurement techniques is given in Table 1) used in this study is considered to have a sufficiently large error. So, the NO_2 steady state approach is not accurate enough to calculate $[HO_2+RO_2]$ for the measurements considered in this study.

Ground-based (Mihelcic et al., 2003; Kanaya et al., 2007, 2012; Elshorbany et al., 2012; Lu et al., 2012, 2013; Tan et al., 2017,

125   2018; Whalley et al., 2018, 2021; Lew et al., 2020) and airborne (Crawford et al., 1999; Tan et al., 2001; Cantrell et al., 2003b) measurements have also been compared with model simulations of HO_2 and RO_2. The discrepancies encountered depend upon the chemical composition of the air mass and the chemical mechanisms and constraints used in the model simulations. Recently, Tan et al., 2019 and Whalley et al., 2021 reported experimental radical budget calculations using PSS assumption for OH, HO_2 and RO_2 together with the published reaction rate coefficients of the reactions (R1 to R26), which control OH, HO_2 and RO_2 in the

130   lower troposphere, and the ground-based measurements of all relevant reactants and photolysis frequencies. In this study, a similar approach has been used, i.e., the sum of HO_2 and RO_2 is assumed to be in PSS, to calculate the amount of peroxy radicals in the air masses measured on-board of the **H**igh **A**ltitude **Lo**ng range (HALO) research aircraft over Europe during the first campaign of the EMeRGe (**E**ffect of **Me**gacities on the transport and transformation of pollutants on the Regional to Global scal**e**s) project. The available on-board measurements of RO_2^* are defined as the total sum of OH, RO and peroxy radicals (i.e., $RO_2^* = OH + \sum RO$

135 $+ HO_2 + \sum RO_2$, where RO_2 are the organic peroxy radicals producing NO_2 in their reaction with NO). As the amount of OH and RO is much smaller, RO_2^* to a good approximation is the sum of HO_2 and those RO_2 radicals that react with NO to produce NO_2. For the calculation, RO_2^* is assumed to be in PSS, and an analytical expression is developed with a manageable degree of complexity to estimate the concentration and mixing ratios of RO_2^*. The simultaneous on-board measurements of trace gases and photolysis frequencies are used to constrain the estimate of the RO_2^* concentration.

140 In contrast to other experimental deployments, the concentrations and/or mixing ratios of the majority of the key species involved in reactions R1 to R26 were continuously measured on-board HALO during the EMeRGe campaign. This enables the use of a large number of measurements to constrain the PSS calculation of RO_2^*. Consequently, this data set provides an excellent opportunity to gain deeper insight into the source and sink reactions of RO_2^* and the applicability of the PSS assumption for the different pollution regimes and related weather conditions in the free troposphere.

145 **2. EMeRGe field campaign in Europe**

The overarching objective of the EMeRGe project is to test and improve the current understanding of the photochemical and heterogeneous processing of pollution outflows from **m**ajor **p**opulation **c**entres (MPCs) and their impact on the atmosphere. Two **i**ntensive **o**bservational **p**eriods (IOP) were carried out to investigate selected European and Asian MPC outflows. The European IOP took place from 10 to 28 July 2017 (http://www.iup.uni-bremen.de/emerge/home/home.html). An extensive set of in-situ and

150 remote-sensing airborne measurements of trace gases and aerosol particles were made on-board the HALO aircraft (see www.halo-spp.de) along flight tracks in the lower layers of the troposphere from northwest Europe to the Mediterranean region.

During EMeRGe in Europe, HALO made a total of 53 flight hours distributed over seven flights to investigate the chemical composition of the outflows from the target MPCs: London, Paris, Benelux/ Ruhr metropolitan area, Po Valley, and urban agglomerations such as Rome, Madrid, and Barcelona. The flight tracks are shown in Fig. 1. All measurement flights started from

155 the aircraft hangar at the DLR in Oberpfaffenhofen, southwest of Munich, Germany. To achieve the scientific goals, 60 % of the flights flew at altitudes below 3000 m. Vertical profiles of trace constituents were typically made by keeping the HALO altitude constant at different at flight levels upwind and downwind of the target MPCs. The flights are named E-EU-FN, where E stands for EMeRGe, EU for Europe, and FN is the two-digit flight number. More details about the EMeRGe IOP in Europe and the set of instruments deployed on-board the HALO aircraft are described elsewhere (Andrés Hernández et al., 2022).

160
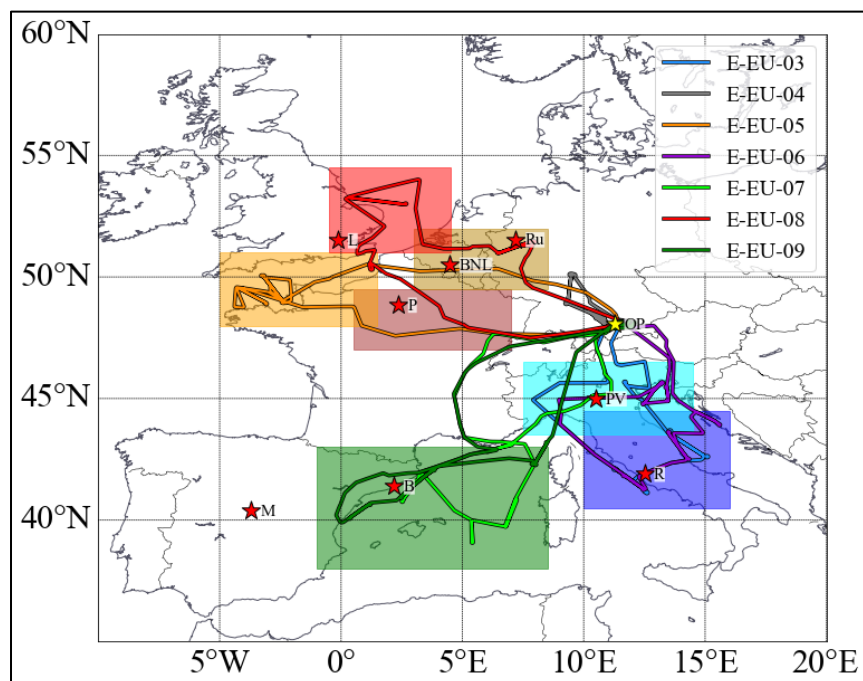
Figure 1: The research flight tracks made by HALO during the EMeRGe-Europe campaign on 11, 13, 17, 20, 24, 26 and 28 July 2017 (E-EU-03 to E-EU-09, respectively, colour coded). MPC target areas are colour coded by shading, and the targeted locations/regions are marked with red stars, M: Madrid, B: Barcelona, P: Paris, L: London; BNL: BeNeLux; Ru: Ruhr area; PV: Po Valley, R: Rome. The location of the aircraft hangar at the DLR in Oberpfaffenhofen, Germany (OP) is indicated by a yellow star.

165

3. PeRCEAS and other instruments on-board HALO during EMeRGe

The RO_2^* measurements on-board the HALO research aircraft during EMeRGe were made using the **Pe**roxy **R**adical **C**hemical **E**nhancement and **A**bsorption **S**pectrometer (PeRCEAS). PeRCEAS combines the **Pe**roxy **R**adical **C**hemical **A**mplification (PeRCA) and **C**avity **R**ing-**D**own **S**pectroscopy (CRDS) techniques in a dual-channel instrument. Each channel has a separate

170 chemical reactor and detector, which operate alternatively in both background and amplification modes to account for the rapid background variations during airborne measurements. In both modes NO is continuously added to the air sampled at the reactor, while CO is only added in the amplification mode to initiate the chain conversion of RO_2^* into NO_2. In the amplification mode, the sum of the NO_2 produced from ambient RO_2^* through the chain reaction, the ambient NO_2, the NO_2 produced from the ambient $O_3 - NO$ reagent gas reaction and the NO_2 produced in the inlet from any other sources (e.g., thermal decomposition of PAN) is

175 measured. In the background mode, the sum of the ambient NO_2, the NO_2 produced from the ambient $O_3 - NO$ reagent gas reaction and NO_2 produced in the inlet from any other sources is measured. The RO_2^* is retrieved by dividing the difference in NO_2 concentration (ΔNO_2) between amplification and background mode by the conversion efficiency of RO_2^* to NO_2, which is referred to as eCL (**e**ffective **c**hain **l**ength). The PeRCEAS instrument and its specifications have been described in detail elsewhere (Horstjann et al., 2014, George et al., 2020).

180 The two chemical reactors for sampling the ambient air are part of the **DU**al channel **A**irborne peroxy radical Chemica**l** Amplifi**er** (DUALER) inlet installed inside a pylon located on the outside of the HALO fuselage. During the EMeRGe campaign in Europe, a reagent gas mixing ratio of 30 ppmv NO ([NO] = 1.46 $\times10^{14}$ molecules cm^{-3} at 296 K, 200 mbar) and of 9 % CO ([CO] = 4.4 $\times10^{17}$ molecules cm^{-3} at 296 K, 200 mbar) were added to the sample flow for the chemical conversion of RO_2^* to NO_2. The DUALER inlet was operated at an internal pressure of 200 mbar to achieve stable chemical conversion. The HO_2 and RO_2 detection

sensitivity depends on the rates of loss of HO_2 and RO_2 by the reactions R19 and R22. The latter depend on the concentration of the reagent gas NO added and the reactions rate coefficients, where k_{22} is larger than k_{19}. The average eCL for a 1:1 HO_2 to CH_3O_2 mixture under the DUALER conditions during the campaign in Europe was determined to be 50 ± 8 from laboratory calibrations, where the error is the $\pm 1\sigma$ standard deviation estimated from the reproducibility of the experimental determinations. Likewise, the ratio $\alpha = eCL_{CH_3O_2}/eCL_{HO_2}$ was determined to be 65% for the measurement conditions (George et al., 2020). The values obtained from calibrations before and after the campaign agreed within their experimental errors.

Although the DUALER pressure is kept constant below the ambient pressure, variations in dynamical pressure > 10 mbar during the flight change the residence time and induce turbulences inside the inlet (Kartal et al., 2010; George et al., 2020). These may lead to different physical losses of radicals before amplification and affect the eCL. In the measurements presented in this study, variations in dynamical pressure of this magnitude were only encountered during flight level changes of the aircraft. When used during the analysis, these data sets are either excluded or flagged (P_flag). The effect of the ambient air humidity on eCL (Mihele and Hastie, 1998; Mihele et al., 1999; Reichert et al., 2003) has been accounted for by a calibration procedure reported in George et al. (2020). The $[H_2O]$ in the DUALER inlet was lower than 1×10^{17} molecules cm^{-3} for 60 % of measurements during EMeRGe in Europe, for which the $eCL_{wet} = 76$ % of eCL_{dry}. At the highest humidity observed during the campaign, i.e., $[H_2O]_{inlet} = 2 \times 10^{17}$ molecules cm^{-3}, the eCL_{wet} is 55 % of eCL_{dry} (see Fig. S1 in the supplementary information).

In addition to the measurement of RO_2^* from PeRCEAS, other in-situ and remote-sensing measurements and basic aircraft data from HALO are used in this study. Details of the corresponding instruments are summarised in Table 1. The remote sensing instruments used on HALO during EMeRGe were the mini–Differential Optical Absorption (minDOAS) and the Heidelberg Airborne Imaging DOAS Instrument (HAIDI). The miniDOAS observes the atmosphere using six telescopes: two being optimised for the ultraviolet, two for the visible, and two for the near infrared. Three telescopes observe in nadir viewing and three in limb viewing. The three limb scanning telescopes point to the starboard side perpendicular to the aircraft fuselage axis. They are rotated to compensate for roll relative to the horizon. A variant of the DOAS retrieval technique uses least square fitting of the measured and radiative transfer modelled absorption along the line of sight to retrieve the differential Slant Column Density (dSCD) of the target gas and a scaling reference gas. The latter is the dimer of molecular oxygen (O_4). As the vertical profile of the concentrations of O_2 and thus O_4 are known then the mixing ratios of the target gas at the flight altitude is obtained from the target gas and O_4 dSCDs (for more details see Stutz et al., 2017; Hüneke et al., 2017; Kluge et al., 2020; Rotermund et al., 2021). The HAIDI nadir observations are used to retrieve dSCDs below the aircraft. The dSCDs from HAIDI are then converted to mixing ratios using knowledge of the aircraft altitude and the corresponding geometric Air Mass Factor (AMF), calculated by a radiative transfer model under a well-mixed NO_2 layer assumption. As a result of this assumption, the calculated mixing ratios for HAIDI target gases are lower limits and similar to the actual values while flying within and close to a well-mixed boundary layer. In spite of the differences in sampling volume and temporal and spatial resolution between the in-situ and remote sensing measurement techniques, the concentration of the gas HCHO measured by both techniques were in good agreement and the concentrations of the NO_2 (remote sensing) and NO_y (in situ) were consistent (for more details see Schumann, 2020).

Table 1: List of the airborne measurements and instrumentation used in this study. PeRCA: Peroxy Radical Chemical Amplification; CRDS: Cavity Ring-Down Spectroscopy; PTR-MS: Proton-Transfer-Reaction Mass Spectrometer; AT-BS: Adsorption Tube and Bag air Sampler; TD-GC-MS: Thermal Desorption Gas Chromatography and Mass Spectrometry; DOAS: Differential Optical Absorption Spectrometry; Univ: University; KIT: Karlsruher Institut für Technologie; DLR: Deutsches Zentrum für Luft- und Raumfahrt; IPA: Institut für Physik der Atmosphäre; FZ: Forschungszentrum; FX: Flugexperimente.

Trace gas-in situ measurements				
Species/parameters	Acronym	Institution	Technique/Instrument	Reference
$RO_2^* = HO_2 + \sum RO_2$	PeRCEAS	Univ. Bremen	PeRCA + CRDS	George et al., 2020
OVOC	HKMS	KIT Karlsruhe	PTR-MS	Brito and Zahn, 2011
O_3	FAIRO	KIT Karlsruhe	UV-Photometry/ Chemiluminescence	Zahn et al., 2012
O_3, CO	AMTEX	DLR-IPA	UV-Photometry/ VUV-Fluorimetry	Gerbig et al., 1996
NO, NO_y	AENEAS	DLR-IPA	Chemiluminescence/ Gold converter	Ziereis et al., 2004
CO_2, CH_4	CATS	DLR-IPA	CRDS	Chen et al., 2010
Trace gas- remote sensing measurements				
Species/parameters	Acronym	Institution	Technique/Instrument	Reference
NO_2, HONO, CH_2O, $C_2H_2O_2$, $C_3H_4O_2$	miniDOAS	Univ. Heidelberg	DOAS / UV-nIR; 2D optical spectrometer	Hüneke et al., 2017
NO_2	HAIDI	Univ. Heidelberg	DOAS / 3x2D-imaging spectrometers	General et al., 2014
Other parameters				
Species/parameters	Acronym	Institution	Technique/Instrument	Reference
Spectral actinic flux density (up/down) Photolysis frequencies	HALO-SR	FZ Jülich	CCD spectro-radiometry	Bohn and Lohse, 2017
Basic aircraft data	BAHAMAS	DLR-FX	various	Mallaun et al., 2015

4. Results and discussion

4.1. Airborne RO_2^* measurements during EMeRGe in Europe

RO_2^* mixing ratios up to 120 pptv were measured during the campaign, as shown in Fig. 2. Typically, the highest RO_2^* mixing ratios were observed below 3000 m over Southern Europe.
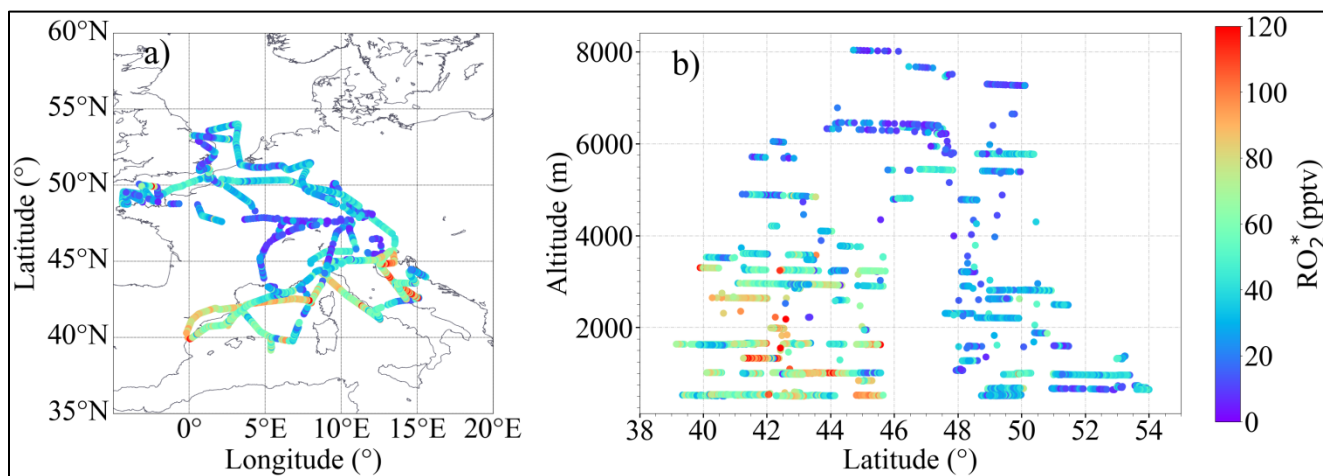
Figure 2: RO$_2^*$ measured during EMeRGe-Europe: a) as a function of longitude and latitude, b) as a function of latitude and altitude.

The origin and thus the composition of the air sampled during the seven flights over Europe were different and heterogeneous. Typically, the air masses measured were influenced by emissions from MPCs and their surroundings, and sometimes by biomass burning transported over short or long distances. The concentration and mixing ratio of RO$_2^*$ rather depends on the insolation and the chemical composition of the air probed, particularly on the abundance of RO$_2^*$ precursors, than on the origin of the air masses. Since RO$_2^*$ are controlled by fast chemical and photochemical processes, the air mass origin and trajectory are not used in the calculation of RO$_2^*$ concentrations and mixing ratios but are of interest as the source of . RO$_2^*$ precursors. Thus, the RO$_2^*$ variability and its production rates provide valuable insight into the photochemical activity of the air masses probed.

Changes in RO$_2^*$ as a function of latitude and altitude, as shown in Fig. 2, confirm the heterogeneity of the photochemical activity in the air masses probed. Figure 3 shows the RO$_2^*$ vertical profiles averaged for the EMeRGe flights over Europe in 500 m altitude bins. The error bars are standard errors (i.e., $\pm$ 1σ standard deviation of each bin). The vertical profiles may be biased as the higher altitudes have fewer measurements than those below 3000 m, as mentioned in section 2. The vertical profiles are a composite from averaging flights with legs carried out at different longitude and latitudes, and are only shown to summarise the variability in the composition of the air masses measured during the campaign.
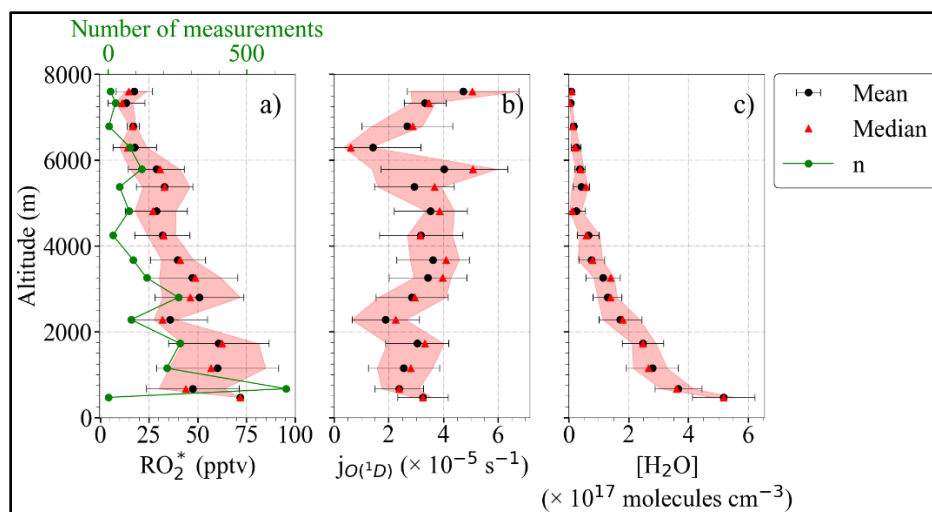
Figure 3: Composite average vertical profiles of a) RO$_2^*$, b) j$_{O(^1D)}$ and c) [H$_2$O] observations. The measurements are binned over 500 m altitude. The error bars are the $\pm$ 1σ standard deviation of each bin. Median values (red triangles) the interquartile 25-75% range (red-shaded area) and the number of individual measurements, n, for each bin (in green) are additionally plotted.

250   Most of the EMeRGe measurements below 2000 m were carried out in the outflow of MPCs, which are expected to contain significant amounts of RO_2^* precursors. HALO flew at the lowest altitudes during flight legs over the English Channel, the Mediterranean and the North Sea. The H_2O concentration in the air masses decreases steadily with altitude as expected. The higher relative variability in H_2O observed at 3000 m and the increase at 5000 m is associated with measurements under stormy conditions, often over the Alps.

255   **4.2. RO_2^* production rates**

The rate of production of RO_2^* from the reactions R1 to R13 is given by:

$$P_{RO_2^*} = 2jO_D^1[O_3]\frac{k_{O_D^1 + H_2O}[H_2O]}{k_{O_D^1 + H_2O}[H_2O] + k_{O_D^1 + O_2}[O_2] + k_{O_D^1 + N_2}[N_2]} + j_{HONO}[HONO] + 2j_{H_2O_2}[H_2O_2] + 2\sum_i j_i[OVOC_i] +$$

$$+\sum k_{O_3 + alkenes_k}[O_3][alkenes_k]\gamma_k \hspace{4cm} (Eq. 2)$$

where OVOC stands for oxygenated volatile organic compounds and γ is the effective RO_2^* yield from ozonolysis of alkenes.

260   In this study, Eq. 2 has been applied to the measurements taken within the EMeRGe campaign in Europe. There were no H_2O_2 measurements available for EMeRGe. However, the results reported by Tan et al. (2001), indicate that the rate of OH production from the H_2O_2 photolysis is not significant except when NO_x is low. To be more precise, for conditions having NO < 50 ppt, the partitioning of HO_x is strongly shifted to HO_2. HO_2 then predominantly reacts with itself or RO_2 to form peroxides, which can in turn photolyse. For conditions with NO > 50 pptv the rates of reactions of HO_x with NO_x are faster than those of HO_2 with HO_2

265 and RO_2. As the NO mixing ratio was higher than 50 pptv in 75 % of the air masses probed in Europe, the rate of the photolysis of H_2O_2 was as a first approximation assumed not to be significant source of OH for the EMeRGe dataset considered in this study.

Formaldehyde (HCHO), acetaldehyde (CH_3CHO), acetone, ($CH_3C(O)CH_3$), and glyoxal (CHOCHO) were the OVOCs measured in EMeRGe forming directly radicals through photolysis. They are produced in the photolysis and oxidation of VOCs and are likely the most abundant and reactive OVOCs present. In this study they were assumed to be the dominant VOCs in the air masses

270 probed.

There were no measurements of alkenes provided in EMeRGe. Consequently, the ozonolysis term in Eq. 2 was not included in the analysis.

The above assumptions lead to Eq. 3, which calculates the RO_2^* production rate ($P_{RO_2^*}$) for the EMeRGe measurements as follows:

$$P_{RO_2^*} = 2j_{O(^1D)}[O_3]\frac{k_{O_D^1 + H_2O}[H_2O]}{k_{O_D^1 + H_2O}[H_2O] + k_{O_D^1 + O_2}[O_2] + k_{O_D^1 + N_2}[N_2]} + j_{HONO}[HONO] + 2j_{HCHO}[HCHO] + 2j_{CH_3CHO}[CH_3CHO] +$$

275 $$2j_{CH_3C(O)CH_3}[CH_3C(O)CH_3] + 2j_{CHOCHO}[CHOCHO] \hspace{3cm} (Eq.3)$$

The production rate of RO_2^* molecules can be expressed in units of mixing ratio of RO_2^* by dividing with the air concentration at each altitude, calculated from the pressure and temperature measurements (for the vertical profile and the latitudinal distribution of $P_{RO_2^*}$ see Fig. S2 and S3 in the supplementary information). Figure 4 shows the composite averaged vertical profile of all measured RO_2^* mixing ratios colour-coded with the calculated $P_{RO_2^*}$. For the sake of representativeness and comparability, the

280 number of measurements in each altitude bin is shown in Fig. 4b. The higher RO_2^* mixing ratios observed below 4000 m are typically associated with $P_{RO_2^*} \geq$ 0.4 pptv s^{-1}. Above 4000 m both $P_{RO_2^*}$ and RO_2^* start to decrease with altitude, as expected. This

is related to the decrease in H_2O and other radical precursor concentrations with altitude, as detailed in Fig. 5 and Fig. 6. In previous airborne campaigns at various parts of the world, RO_2^* vertical distributions showed a local maximum between 1500 and 4000 m, as reported by Tan et al. (2001), Cantrell et al. (2003a, 2003b), and Andrés-Hernández et al. (2009). In the present work, this local maximum is more evident for measurements with $P_{RO_2^*} \geq 0.5$ pptv s^{-1}.
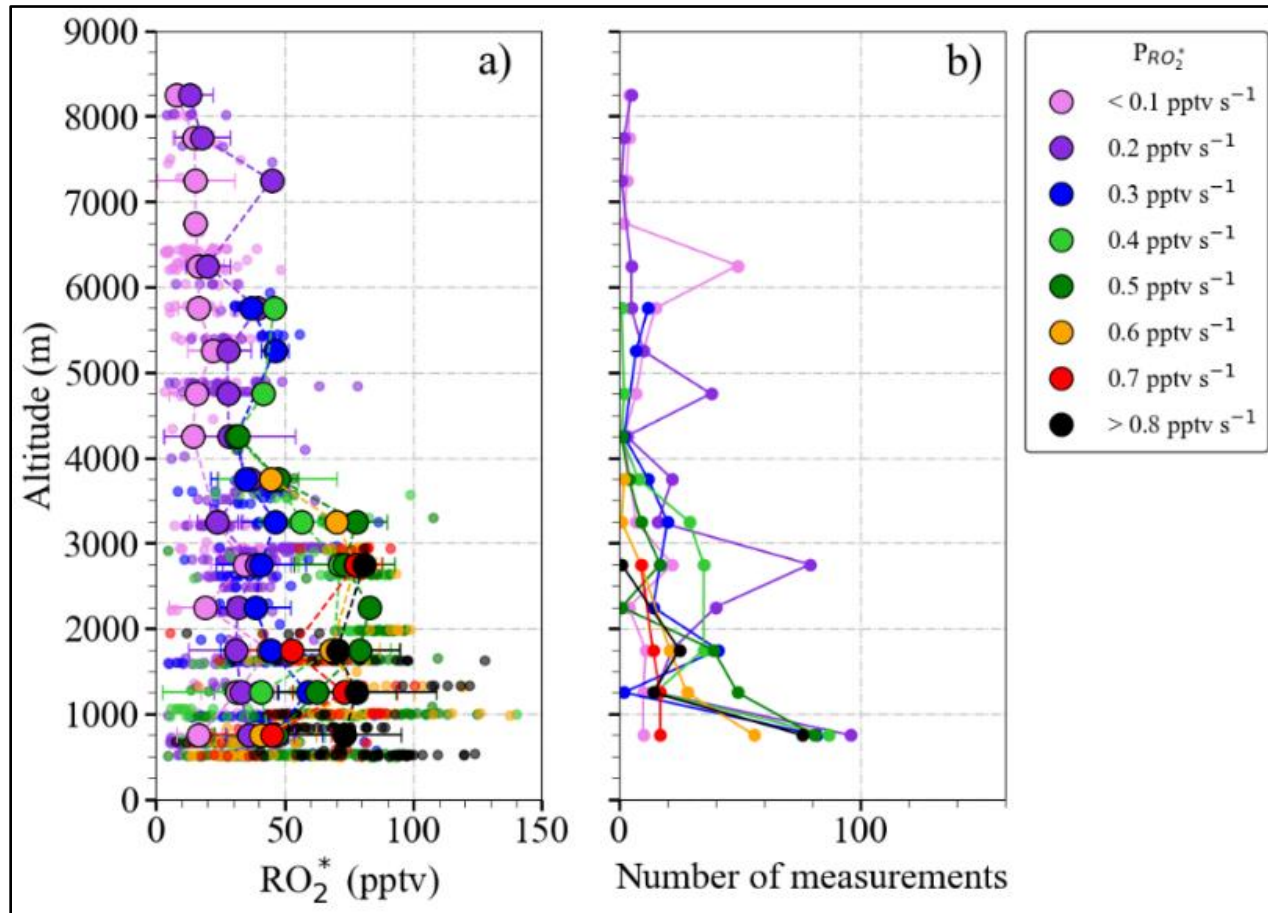
Figure 4: a) Composite averaged vertical distribution of measured RO_2^* colour-coded according to the value of $P_{RO_2^*}$, b) the number of measurements in each altitude bin. Small circles are 1-minute individual measurements binned with $P_{RO_2^*}$ values in 0.1 pptv s^{-1} intervals. Larger circles result from a further binning over 500 m altitude steps. All the production rates below 0.1 pptv s^{-1} and above 0.8 pptv s^{-1} are binned to 0.1 pptv s^{-1} and 0.8 pptv s^{-1}, respectively. The error bars are the standard deviation for each altitude bin.

Figure 5 shows the fractional contribution of the production rate from each radical precursor reaction included in Eq. 3 as a function of altitude. The data are classified into three groups according to the rate of change of production of the RO_2^* mixing ratio $P_{RO_2^*} <$ 0.07 pptv s^{-1} (5a), $0.07 < P_{RO_2^*} < 0.8$ pptv s^{-1} (5b), and $P_{RO_2^*} > 0.8$ pptv s^{-1} (5c) to show the lowest, most common, and highest ranges, respectively, encountered during the campaign. For 89 % of the measurements, $0.07 < P_{RO_2^*} < 0.8$ pptv s^{-1} applies, while the rest of the data are equally distributed in the other two $P_{RO_2^*}$ ranges. The data in each group are always binned over 500 m when available.

Typically, the high amount of H_2O in the air masses probed leads to the reaction of O^1D with H_2O (reactions R1-R2a) being the highest RO_2^* radical production rate ($\geqslant 50$ %) below 4000 m. As the amount of H_2O reduces with altitude, the relative contribution from O_3 photolysis decreases. Above 4000 m, HCHO, HONO, and CHOCHO photolysis contributions range between 20 % to 40 %, 2.5 % to 30 %, and 5 % to 25 %, respectively. The HCHO contribution increases up to 80% during measurements above 6000 m. The contributions of CH_3CHO and $CH_3C(O)CH_3$ photolysis are, in contrast, practically negligible (< 5 %).

The vertical changes of the precursor mixing ratios and photolysis frequencies used to calculate $P_{RO_2^*}$ in Fig. 5 are shown in Fig. 6a to 6f. $P_{RO_2^*} < 0.07$ pptv s^{-1} is associated with measurements under cloudy conditions, towards sunset where the photolysis frequencies are low, or at altitudes above 5000 m in air masses with a low amount of RO_2^* precursors. $P_{RO_2^*} > 0.8$ pptv s^{-1} are found for air masses, measured below 2000 m in the outflow of MPCs over the sea, for conditions having sufficient insolation ($j_{O(^1D)} > 3 \times 10^{-5}$ S^{-1}) and a high content of RO_2^* precursors (HCHO > 1000 pptv and HONO >100 pptv). The increase in the photolysis frequencies as a function of altitude is concurrent with decreases in precursor concentrations. As a result, the $P_{RO_2^*}$ do not significantly vary with altitude in the air masses investigated.

In previous airborne campaigns, Tan et al. (2001) and Cantrell et al. (2003b) reported a reduction of the fractional contribution of the reaction of O(^{1}D) with H_2O as the $P_{RO_2^*}$ value decreases. At very low $P_{RO_2^*}$ values (< 0.03 pptv s^{-1}), the sum of all other production terms exceeded the fraction from the O(^{1}D) + H_2O term. For these conditions, H_2O_2 and VOCs photolysis dominated the $P_{RO_2^*}$. For the EMeRGe data set in Europe, only 6 % of $P_{RO_2^*}$ are below 0.06 pptv s^{-1}.
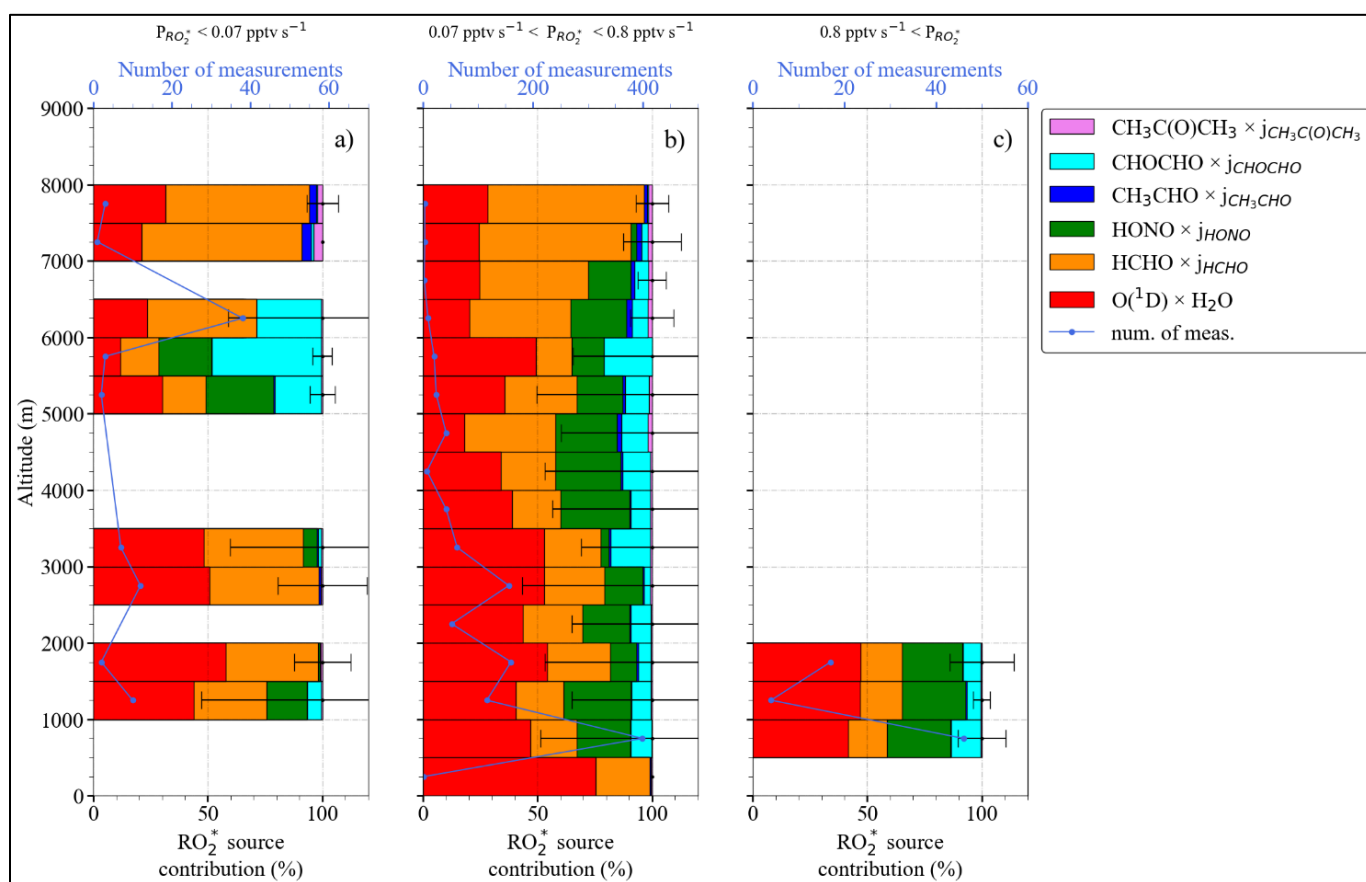
Figure 5: Total $P_{RO_2^*}$ and fractional precursor contributions estimated using Eq. 5 as a function of altitude, for: a) $P_{RO_2^*} < 0.07$ pptv s^{-1}, b) 0.07 pptv s^{-1} < $P_{RO_2^*} < 0.8$ pptv s^{-1}, and c) $P_{RO_2^*} > 0.8$ pptv s^{-1}. Note the different scales in the number of measurements.
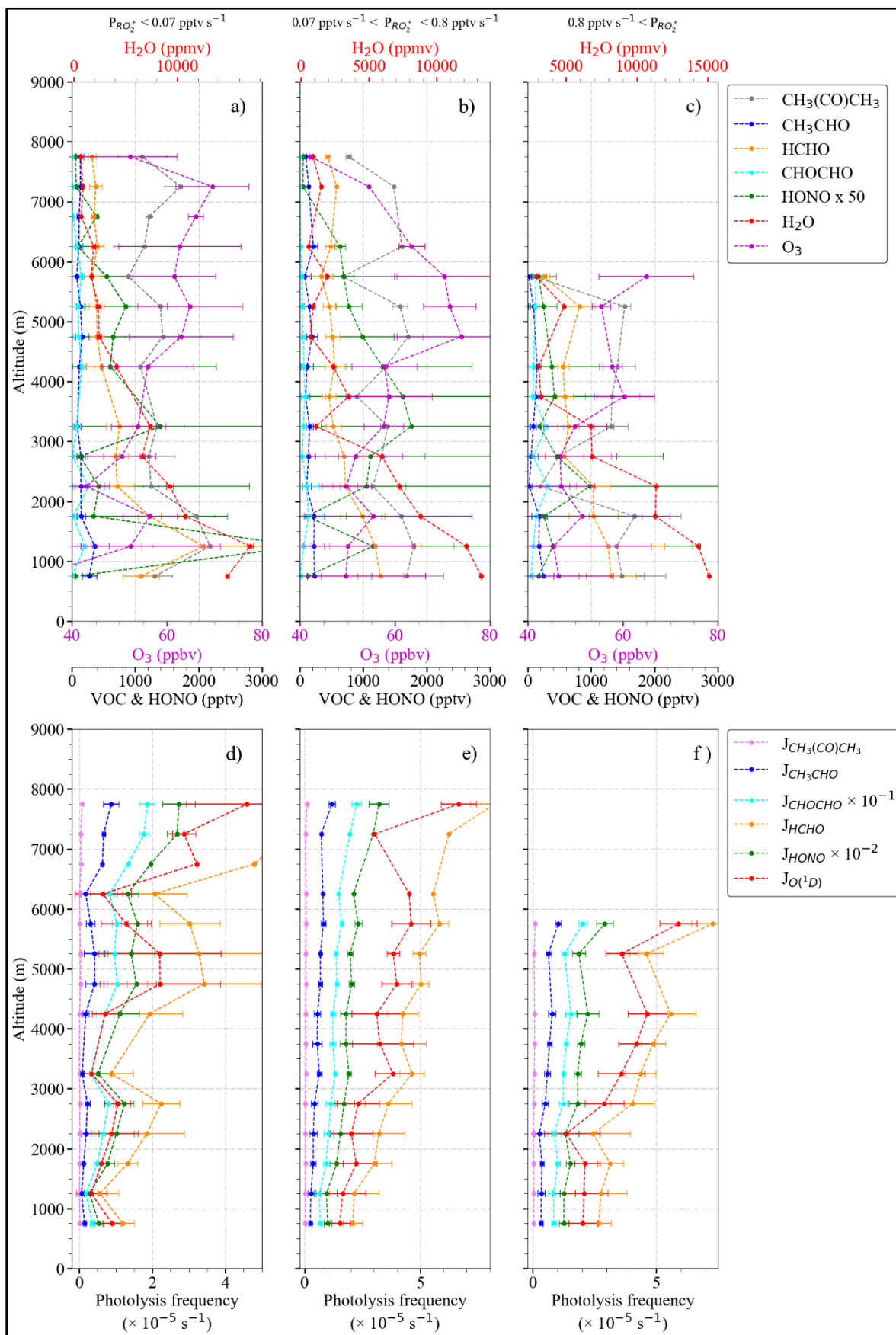
Figure 6: Vertical distribution and variation of a) to c) precursor mixing ratios; d) to f) photolysis frequencies for the $P_{RO_2^*}$ bins as in Fig. 5. Note the different scales in the H_2O concentration

4.3. PSS estimation of the RO_2^* mixing ratios

Under most ambient conditions in the troposphere, the RO_2^* are short-lived, and the chemical lifetime of RO_2^* is much shorter than the chemical transport time into and out of an air mass being probed. Consequently, pseudo-steady-state conditions prevail, and the radical production and destruction rates are balanced:

325

$$P_{RO_2*} = D_{RO_2*} \tag{Eq.4}$$

The reactions R5 to R7, R12, R16b, and R23 to R26 are interconversion reactions between OH, RO, HO_2 and RO_2 and do consequently occur without radical losses. Solving Eq. 4 leads to Eq. 5 if $RO_2^* - RO_2^*$ reactions are assumed to be the dominant radical terminating processes.

330

$$2j_{O(^1D)}[O_3] \frac{k_{O_D^1 + H_2O}[H_2O]}{k_{O_D^1 + H_2O}[H_2O] + k_{O_D^1 + O_2}[O_2] + k_{O_D^1 + N_2}[N_2]} + j_{HONO}[HONO] + 2j_{HCHO}[HCHO] + 2j_{CH_3CHO}[CH_3CHO]$$
$$+ 2j_{CH_3C(O)CH_3}[CH_3C(O)CH_3] + 2j_{CHOCHO}[CHOCHO] = k_{RO_2^* + RO_2^*}[RO_2^*]^2$$

$$\tag{Eq. 5}$$

where j_{HCHO}, j_{CH_3CHO}, $j_{CH_3C(O)CH_3}$, j_{CHOCHO} are respectively j_8, j_9, $j_{10a,b}$ and j_{11}, as in Table 1 in the supplementary information. and $k_{RO_2^* + RO_2^*}$ represents an effective RO_2^* self-reaction rate coefficient, comprising $HO_2 - HO_2$, $HO_2 - RO_2$ and $RO_2 - RO_2$ reaction

335 rates.

Consequently, the RO_2^* concentrations are expected to correlate with the square root of the $P_{RO_2^*}$.

Figure 7 shows the relationship between the measured $[RO_2^*]$ and the calculated $\sqrt[2]{P_{RO_2^*}}$. Generally, both $[RO_2^*]$ and $\sqrt[2]{P_{RO_2^*}}$ increase with the photolysis frequency of O_3 ($j_{O(^1D)}$). Measurements in which $[RO_2^*]$ were less than 0.5×10^{12} molecules cm^{-3}, $\sqrt[2]{P_{RO_2^*}}$ less than 1000 and with $j_{O(^1D)} > 5 \times 10^{-5}$ were made above 6000 m, where the amount of RO_2^* precursors is low. The

340 relatively weak correlation observed between $[RO_2^*]$ and $\sqrt[2]{P_{RO_2^*}}$ indicates the necessity of other radical terminating processes and/or missing radical formation terms in the $P_{RO_2^*}$ calculation. Apart from this, the spread in the diagram confirms that the effective RO_2^* self-reaction rate $k_{RO_2^* + RO_2^*}[RO_2^*]^2$ varies widely in the air masses probed likely due to the effect of changes in HO_2 and $\sum RO_2$ concentrations in the individual loss reaction rate coefficients. Photochemical processing is expected to be enhanced over Southern Europe due to the prevailing conditions of high insolation and temperatures during the EMeRGe flights, which might

345 lead to the rapid production of RO_2^* from the photochemical oxidations of CO and VOCs. This is also reflected in the higher $P_{RO_2^*}$ and $[RO_2^*]$ observed in Southern Europe as compared to those in Northern Europe (Fig. 7b).
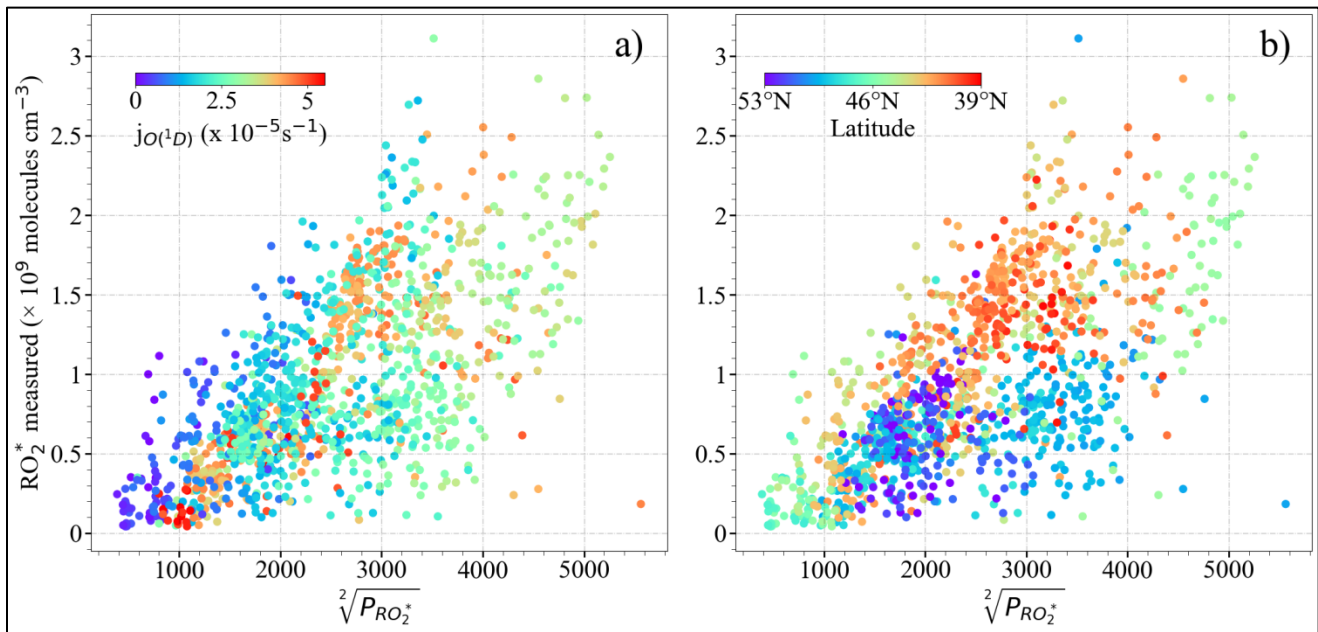
Figure 7: Measured $[RO_2{}^*]$ versus calculated $\sqrt[2]{P_{RO_2^*}}$ colour-coded for values of a) $j_{O(^1D)}$ and b) latitude.

The correlation between $[RO_2{}^*]$ and $\sqrt[2]{P_{RO_2^*}}$ improves when the measurements south and north of 47°N are separately analysed (Fig. 8). For a given $[RO_2{}^*]$, the $P_{RO_2^*}$ calculated is higher for the measurements north of 47°N than south of 47°N. The lowest $[RO_2{}^*]$ to $\sqrt[2]{P_{RO_2^*}}$ ratios are associated with higher NO_x ($NO + NO_2$), especially north of 47°N, indicating the urban character and higher amounts of the $RO_2{}^*$ precursors of the air probed (Fig. 8d). Please note that these results are only valid for the data set acquired over Europe during EMeRGe flights and do not yield a relationship between $[RO_2{}^*]$ and $\sqrt[2]{P_{RO_2^*}}$, which is generally applicable under all conditions for these two latitude windows.
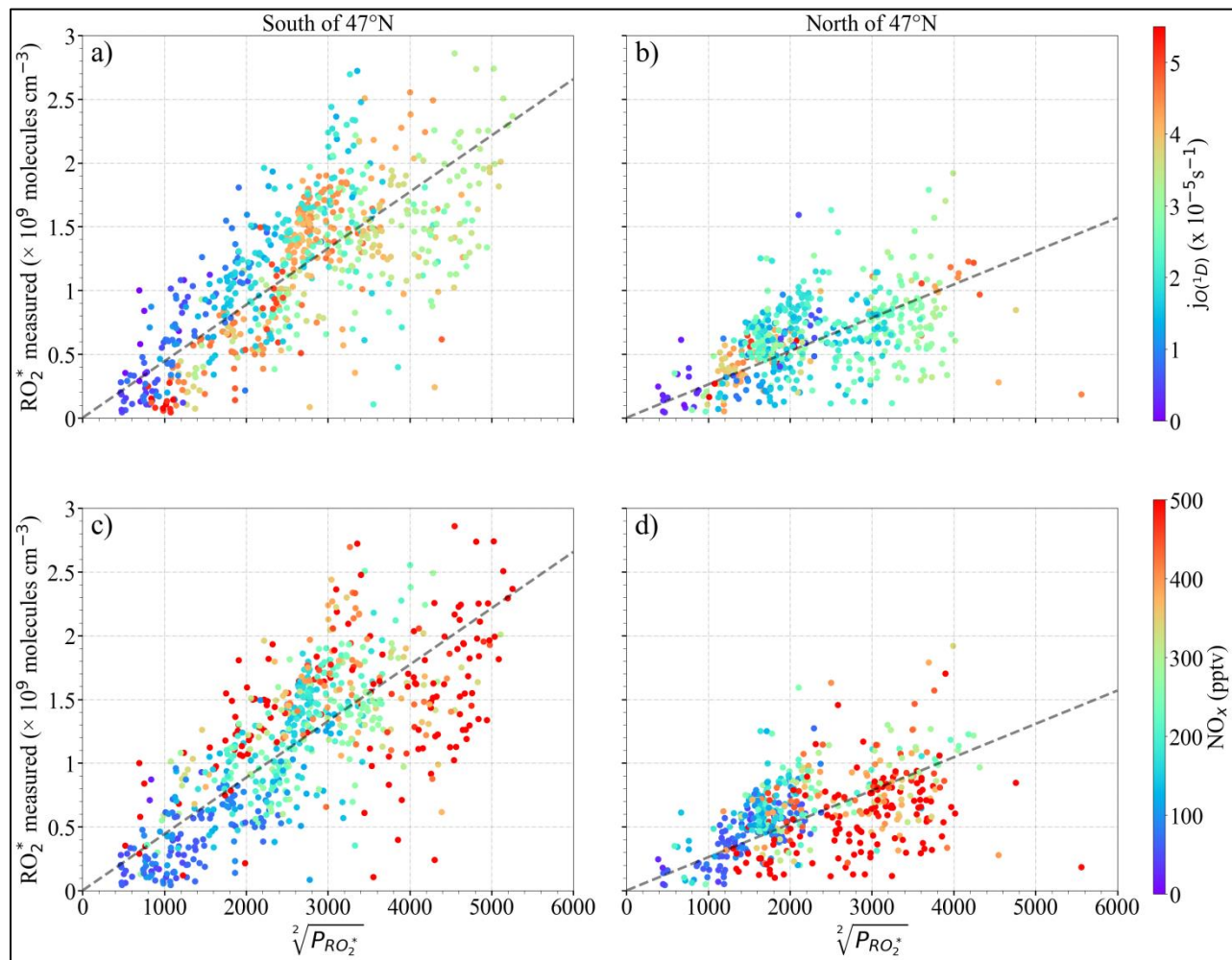
Figure 8: Measured $[RO_2^*]$ vs $\sqrt[2]{P_{RO_2^*}}$ for the following latitudes: a) and c) south of 47°N; b) and d) north of 47°N. Note that a) and b) are colour-coded with $j_{O(^1D)}$; c) and d) are colour-coded by NO_x mixing ratio. The dashed lines indicate the linear fit for visual support.

The relationship between RO_2^* and $P_{RO_2^*}$ is further investigated to identify the dominant RO_2^* loss process in the air masses considered in this study. As stated in section 3, HO_2 and RO_2 are not speciated but retrieved as RO_2^* by the PeRCEAS instrument. Because not all peroxy radicals are detected equally by the instrument, the comparison of measured and calculated RO_2^* values is complicated. To investigate this the changes in the HO_2 to the total RO_2^* ratios have been taken into consideration by δ, i.e., $[HO_2]$ = δ$[RO_2^*]$ and $[CH_3O_2]$ = (1- δ) $[RO_2^*]$, in the analysis. As a first approach, RO_2 is assumed to consist only of CH_3O_2 to reduce the complexity of the calculations by considering only CH_3O_2 reaction rate constants. The reaction channel R25b is not considered in the calculation since the yield of this channel is < 5 % (Burkholder et al., 2020) for CH_3O_2 + NO reaction. Moreover, in a previous study the ratio α = $eCL_{CH_3O_2}/eCL_{HO_2}$ was determined to be 65% for the measurement conditions (George et al., 2020).

The Eq. 5 is additionally extended to include RO_2^* effective yields from VOC oxidation and radical losses through HONO, HNO_3:

$$(2j_1[O_3]\beta + j_3[HONO])(1 - \rho) + 2j_8[HCHO] + 2j_9[CH_3CHO] + 2(j_{10a} + j_{10b})[CH_3C(O)CH_3] + 2j_{11}[CHOCHO] =$$
$$\delta[RO_2^*](k_{23}[NO] + k_{24}[O_3])\rho + 2k_{15}\delta(1 - \delta)[RO_2^*]^2 + 2k_{16a}\big((1 - \delta)[RO_2^*]\big)^2 + 2k_{14}(\delta[RO_2^*])^2 \qquad \text{(Eq. 6)}$$

where β is the effective yield of OH in the reaction of O(^{1}D) with H_2O given by:

$$\beta = \left(\frac{k_{2a}[H_2O]}{k_{2a}[H_2O]+ k_{2b}[O_2]+ k_{2c}[N_2]}\right),$$

On the left-hand side of Eq. 6, 1-ρ accounts for the effective yield of HO_2+RO_2 through the radical initiation reactions R2a and R3 and reactions R5 to R7 and reaction R12. As the calculation is constrained with on-board measurements, only the reactions of measured VOCs were considered in reaction R12. Similarly, on the right-hand side of Eq. 6, ρ accounts for the radical termination through the OH + NO, OH + NO_2, and OH + HONO reactions (reactions R19 to R21) relative to the radical undergoing OH to peroxy radical conversion.

Consequently, ρ is given by:

$$\rho = \frac{(k_{19}[NO]+ k_{20}[NO_2]+k_{21}[HONO])}{(k_5[O_3] +k_6[CO]+ k_7[CH_4]+ k_{12a}[HCHO]+ k_{12b}[CH_3CHO]+ k_{12c}[CH_3C(O)CH_3]+ k_{12d}[CH_3OH] + k_{12e}[CHOCHO]+ k_{17}[HO_2]+ k_{19}[NO]+ k_{20}[NO_2]+k_{21}[HONO])}$$

Measurements of CH_4, HCHO, CH_3CHO, CHOCHO, CH_3OH, and $CH_3C(O)CH_3$ on-board HALO are available and implemented in Eq. 6. These comprise the most abundant and reactive OVOCs and are considered to be a representative surrogate for the VOCs that act as RO_2^* precursors through oxidation and photolysis. During the EMeRGe campaign in Europe, $k_{12a} \times$ HCHO and $k_{12b} \times$ CH_3CHO have the highest contribution to the $1 - \rho$ from all the OVOC measured. Their impact on the RO_2^* budget is found to be similar because their respective concentrations compensate the difference in the rate coefficients of their reactions with OH ($k_{12a} = 8.5 \times 10^{-12}$ cm^3 molecule^{-1} s^{-1} and $k_{12b} = 1.5 \times 10^{-11}$ cm^3 molecule^{-1} s^{-1} at 298K and 1 atm.). Despite its high mixing ratios measured, $CH_3C(O)CH_3$ is less important in the $1 - \rho$ term. This is because the rate coefficient $k(T)_{12c}$ is significantly slower than k_{12a} and k_{12b} (see Table S1 in the supplement). Similarly, the contribution of CHOCHO and CH_3OH is an order of magnitude lower than that of HCHO and CH_3CHO.

Concerning the term $\delta[RO_2^*](k_{23}[NO] + k_{24}[O_3])\rho$ on the right hand side of Eq.6, the HO_2 reaction with O_3 has a negligible effect as k_{24} is almost four orders of magnitude smaller than k_{23} and the NO concentrations remained about three orders of magnitude smaller than the O_3 measured during the campaign.

The impact of the methylglyoxal ($CH_3C(O)C(O)H$) photolysis was also investigated by using the $CH_3C(O)C(O)H^*$ measurements provided by the miniDOAS instrument. The $CH_3C(O)C(O)H^*$ measured is the sum of $CH_3C(O)C(O)H$, and a fraction of other substituted dicarbonyls (mainly 2,3-butanedione, $C_3H_6O_2$), with similar visible absorption spectra. For the calculation, $CH_3C(O)C(O)H$ was assumed to be half of $CH_3C(O)C(O)H^*$ as recommended by Zarzana et al. (2017) and Kluge et al. (2020). The RO_2^* calculated by including $CH_3C(O)C(O)H$ photolysis systematically overestimated the measurements. As the adequacy of the recommended factor of 0.5 varies with the actual air mass composition, $CH_3C(O)C(O)H$ was not included in the calculations.

Figure 9 shows the fractional contribution of the destruction rate ($D_{RO_2^*}$) calculated for a 1:1 mixture of HO_2 and CH_3O_2 using the reactions included in Eq. 6 as a function of altitude. The data are classified into three groups according to the rate of destruction of RO_2^* mixing ratio $D_{RO_2^*} < 0.01$ pptv s^{-1} (a), $0.01 < D_{RO_2^*} < 0.9$ pptv s^{-1} (b), and $D_{RO_2^*} > 0.9$ pptv s^{-1} (c) to show the lowest, most common, and highest ranges, respectively, encountered during the EMeRGe campaign. For 90 % of the measurements, $0.01 < D_{RO_2^*} < 0.9$ pptv s^{-1} applies, while the rest of the data are equally distributed in the other two $D_{RO_2^*}$ ranges. The data in each group are always binned over 500 m when available.

As can be seen in Fig. 9, the ±1σ standard deviation of the obtained bins is very high. In spite of this, the $HO_2 - CH_3O_2$ and $HO_2 - HO_2$ reactions seem to dominate the radical destruction processes in the air masses probed. Their combined contribution is > 70

% in all the cases except in the 1000 m bin of $D_{RO_2^*} > 0.9$ pptv s^{-1}. Other significant radical losses occur through the HONO and HNO$_3$ formation. The contribution of the $CH_3O_2 + CH_3O_2$ reaction to the total RO_2^* destruction rate is < 5 %.".
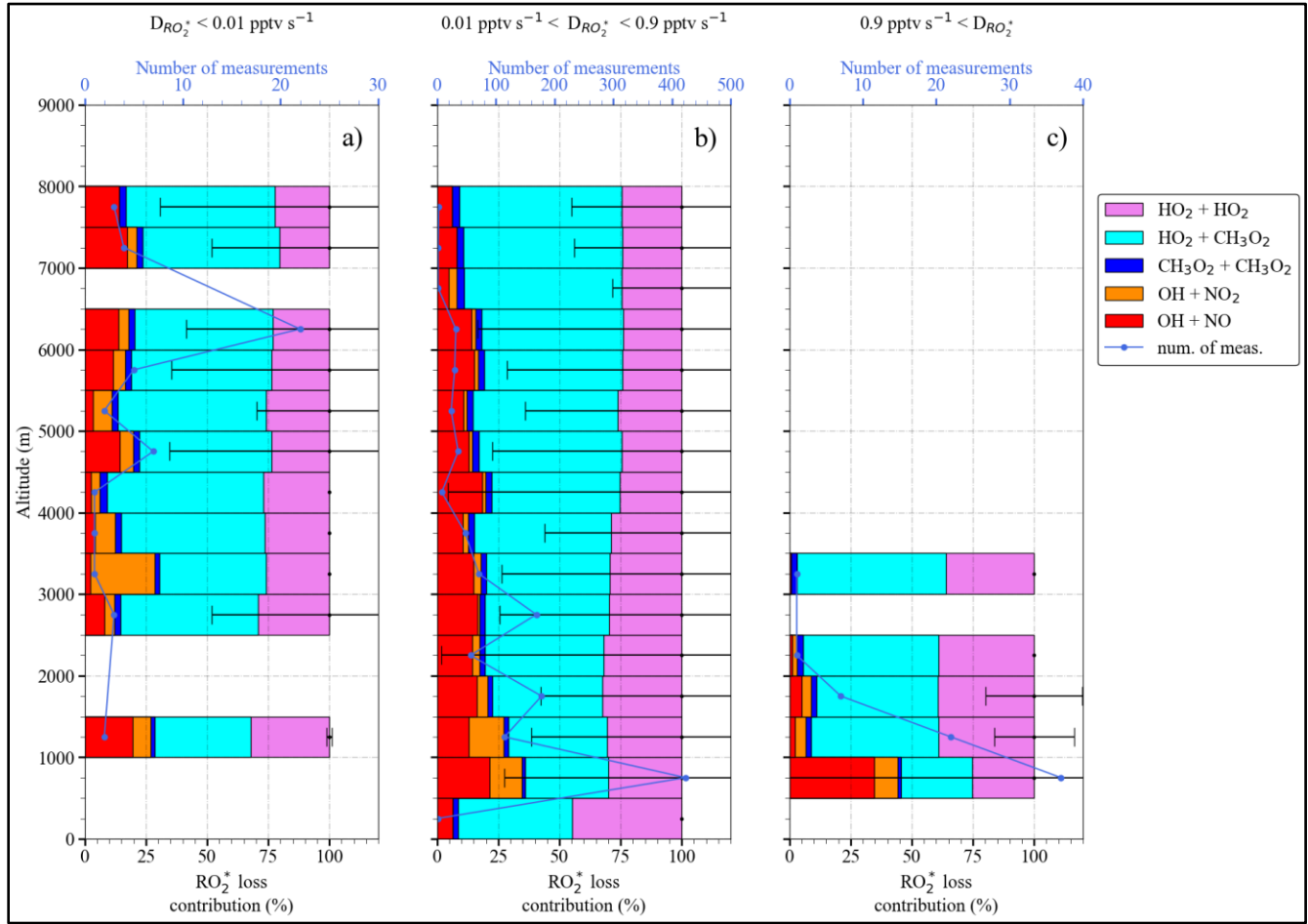
Figure 9: RO_2^* destruction rate $D_{RO_2^*}$ and fractional contributions from loss reactions in Eq.6 as a function of altitude, for: a) $D_{RO_2^*}$ < 0.01 pptv s^{-1}, b) 0.01 pptv s^{-1} < $D_{RO_2^*}$ < 0.9 pptv s^{-1}, and c) $D_{RO_2^*}$ > 0.9 pptv s^{-1}. Note the different scales in the number of measurements.

Since Eq. 6, is quadratic in [RO_2^*] it can be solved for [RO_2^*]$_c$ where c stands for calculated, as:

$$[RO_2^*]_c = \frac{-\left(-L_{RO_2^*}\right) - \sqrt[2]{L_{RO_2^*}^2 - 4\left(-2k_{RO_2^*}\right)P_{RO_2^*}}}{2\left(-2k_{RO_2^*}\right)}$$

(Eq. 7)

where

$$k_{RO_2^*} = \left(k_{16a}(1-\delta)^2 + k_{15}\delta(1-\delta) + k_{14}\delta^2\right)$$

$$L_{RO_2^*} = \left(\delta(k_{23}[NO] + k_{24}[O_3])\rho\right)$$

$$P_{RO_{2g}^*} = (2j_1[O_3]\beta + j_3[HONO])(1-\rho) + 2j_8[HCHO] + 2j_9[CH_3CHO] + 2(j_{10a} + j_{10b})[CH_3C(O)CH_3] + 2j_{11}[CHOCHO]$$

where $k_{RO_2^*}$ is a weighed rate coefficient of RO_2^* self-reactions for a 1:1 mixture of HO_2 and CH_3O_2, $L_{RO_2^*}$ comprises the formation of HONO and HNO$_3$ and $P_{RO_{2g}^*}$ is the gross production of RO_2^*.

The second solution of the quadratic equation gives negative values for [RO_2^*]$_c$, therefore is assumed to have no physical meaning. A more detailed derivation of Eq. 6 and Eq. 7 are given in the supplementary information.

Figure 10 shows the measured RO_2^* (hereinafter referred to as $RO_2^*{}_m$) mixing ratio versus the calculated $RO_2^*{}_c$ mixing ratio using Eq. 7. $RO_2^*{}_m$ and $RO_2^*{}_c$ are the measured and calculated RO_2^* respectively for $\delta = 1$, i.e., $RO_2^* = HO_2$ and $\delta = 0.5$, i.e., $HO_2 = RO_2$. The eCL corresponding to $\delta = 1$ and $\delta = 0.5$ used for the $RO_2^*{}_m$ retrievals were determined in laboratory experiments, as reported

425 by George et al. (2020). The small circles represent 1-minute $RO_2^*{}_m$, whereas the large circles are the mean of the $RO_2^*{}_m$ binned over 10 pptv $RO_2^*{}_c$ intervals. The RO_2^* data are colour-coded with the on-board NO measurements. The linear regression slopes are around 0.7 ($R^2 = 0.96$), indicating an overall 25 – 30 % overestimation of the $RO_2^*{}_m$. The y-axis intercept is below the instrumental detection limit for most measurement conditions. Table 2: Linear regression parameters from $RO_2^*{}_m$ versus $RO_2^*{}_c$ using Eq.7 from Fig.10.

Formula used to calculate RO_2^*	δ	slope	y-intercept (pptv)	R^2
	1.00	0.71	5	0.96
Eq. 7	0.50	0.74	6	0.97

430
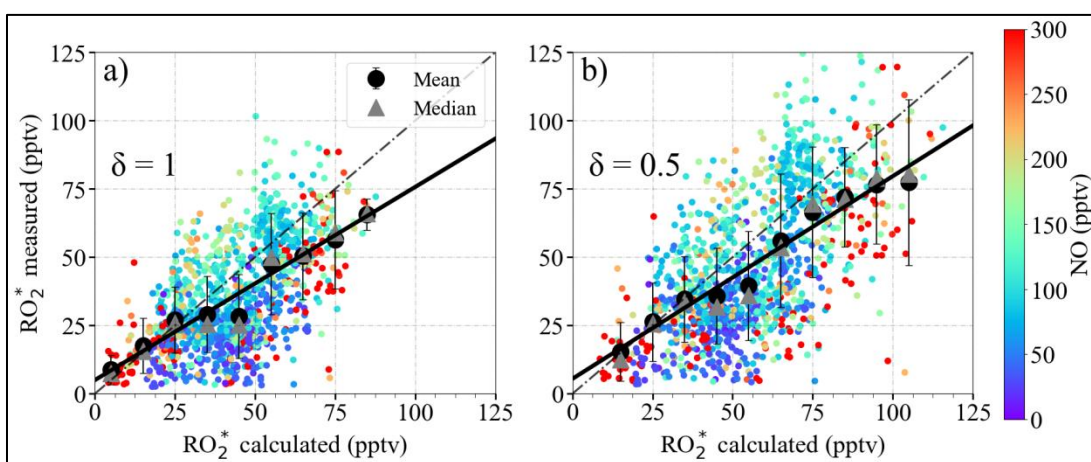
Figure 10: $RO_2^*{}_m$ versus $RO_2^*{}_c$ using Eq. 7 for a) $\delta = 1$ and b) $\delta = 0.5$. The data are colour-coded with the measured NO mixing ratios. The 1-minute (small circles), the mean of the binned $RO_2^*{}_m$ over 10 pptv $RO_2^*{}_c$ intervals (large circles), and the median of each bin (grey triangles) are shown. The error bars indicate $\pm 1\sigma$ standard deviation of each bin. The linear regression for the binned values (solid line) and the 1:1 relation (dashed line) are also depicted for reference.

435 Figure 11 shows the vertical profiles of $RO_2^*{}_m$ and $RO_2^*{}_c$ mixing ratios calculated for $\delta = 0.5$, averaged for the EMeRGe flights over Europe in 500 m altitude bins. $RO_2^*{}_c$ seems to overestimate $RO_2^*{}_m$ for altitudes above 4000 m. As mentioned in Sect. 4.1, the vertical profiles are a composite from averaging flights with legs carried out at different longitude and latitudes. Therefore, the differences between $RO_2^*{}_m$ and $RO_2^*{}_c$ have been studied in more detail respect to the composition of the individual air masses (see the $RO_2^*{}_m$ and $RO_2^*{}_c$ mixing ratios as a function of latitude and altitude in Fig. S4 in the supplementary information).
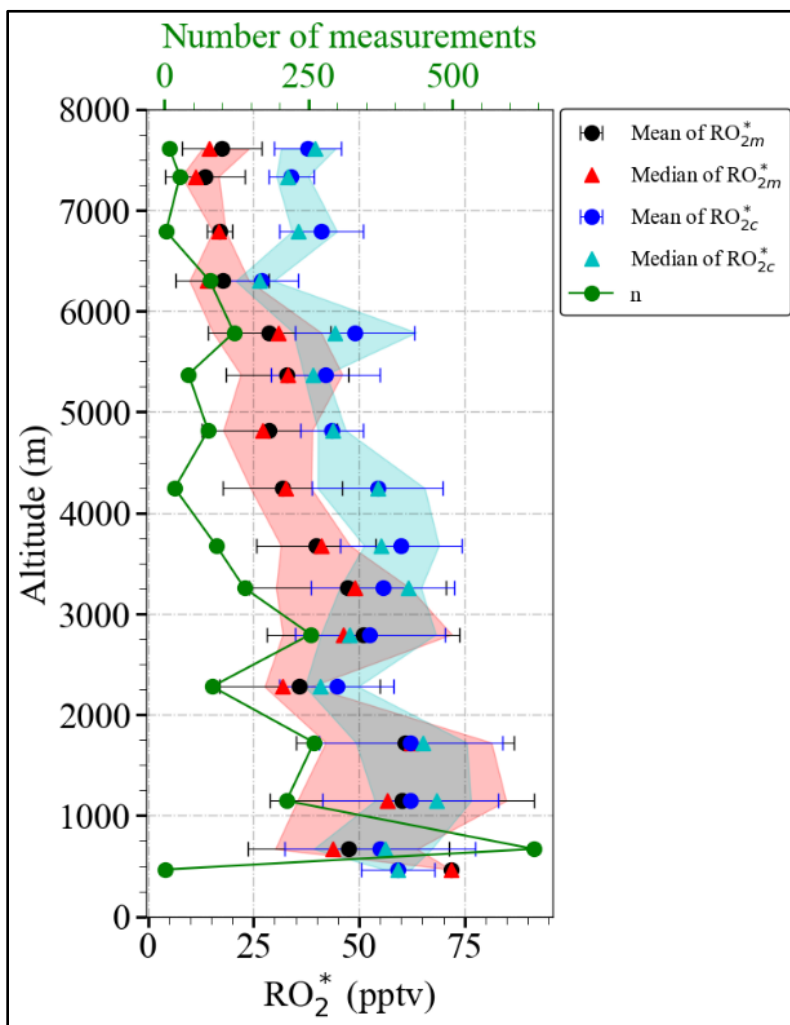
440

Figure 11: Vertical distribution of the mean $RO_2^*{}_m$ and mean $RO_2^*{}_c$ using Eq. 7 for $\delta = 0.5$ for the EMeRGe data set in Europe. The measurements are binned over 500 m altitude. The error bars are the $\pm 1\sigma$ standard deviation of each bin. Median values (red and green triangles) the interquartile 25-75% range (red and blue shaded areas) and the number of individual measurements, n, for each bin (in green) are additionally plotted.

445 Figure 12 shows the data for $\delta = 0.5$ colour-coded with NO, NO_x, the sum of HCHO, CH_3CHO, CHOCHO, CH_3OH, and $CH_3C(O)CH_3$ (from now on referred to as ΣVOCs), as a surrogate for the amount of OVOCs acting as RO_2^* precursors, and the ΣVOCs to NO ratio. The largest differences between $RO_2^*{}_m$ and $RO_2^*{}_c$ are observed for the bins around 50 pptv. The $RO_2^*{}_c$ overestimate the $RO_2^*{}_m$ mostly for $RO_2^*{}_m < 25$ pptv observed above ≈ 4000 m. These air masses are characterised by NO < 50 pptv, ΣVOCs typically below 4 ppbv, high ΣVOCs/NO ratios (> 50), and low insolation conditions, i.e., $j_{O(^1D)} < 2 \times 10^{-5}$ s^{-1} (see

450 Fig. S5 in the supplementary information). Under these insolation conditions, the radical production rate is expected to be low, and the $RO_2^* - RO_2^*$ reactions are expected to dominate the RO_2^* loss processes. As OH and H_2O_2 were not measured during the EMeRGe campaign in Europe, Eq. 7 does not include the loss reactions R17 and R18, which might be significant under such conditions (Tan et al., 2001) and explain the overestimation of $RO_2^*{}_m$. This is also the case for the overestimations observed below 40 pptv $RO_2^*{}_m$ at other altitudes, where NO < 50 pptv but the ΣVOCs/NO ratios remain low. The overestimation may therefore be

455 independent of the ΣVOCs/NO ratios. For NO $\leq$ 50 pptv, $NO_2 \leq$ 100 pptv, $RO_2^* \leq$ 40 pptv and HCHO $\leq$ 1 ppbv, the rate of reaction R17, which forms H_2O and O_2 from OH and HO_2, is about 4 times faster than the rate of the OH oxidation reaction of the dominant OVOCs (reaction R12) considered in this study or the rate of formation of HONO (reaction R19).

$RO_2{}^*_m$ is both underestimated and overestimated for $\sum VOCs$ mixing ratios greater than 7 ppbv. The composition of these air masses is very different, as reflected by the $\Sigma VOCs/NO$ ratios. This implies that Eq. 7 does not capture the peroxy radical yields adequately from the measured VOCs and OVOC in these cases. The differences between $RO_2{}^*_m$ and $RO_2{}^*_c$ may be explained in part by a) changes in OH yields due to additional VOC oxidation processes, which are not in Eq. 7 and/or b) $RO_2{}^*$ production from the photolysis of carbonyls, which were not measured and/or c) $RO_2{}^*$ production from the ozonolysis of alkenes or unidentified biogenic terpene emissions and/or d) overestimation of the loss processes.

In addition, Eq. 7 does not consider the loss of RO_2 through the organic nitrate formation (reaction R25b) which results in an underestimation of radical loss in the presence of RO_2 with higher organic group. Tan et al., 2019 reported changing the yields for organic nitrate formation channel in reaction R25 from 5% to 20% has a small but notable influence on their experimental budget analysis. Similarly, the RO_2 loss through organic nitrate formation which are not included in Eq. 7 might explain the $RO_2{}^*_m$ overestimations for $\sum VOC < 2ppb$ and $\sum VOCs/NO < 20$, and for $NO > 200$ pptv.
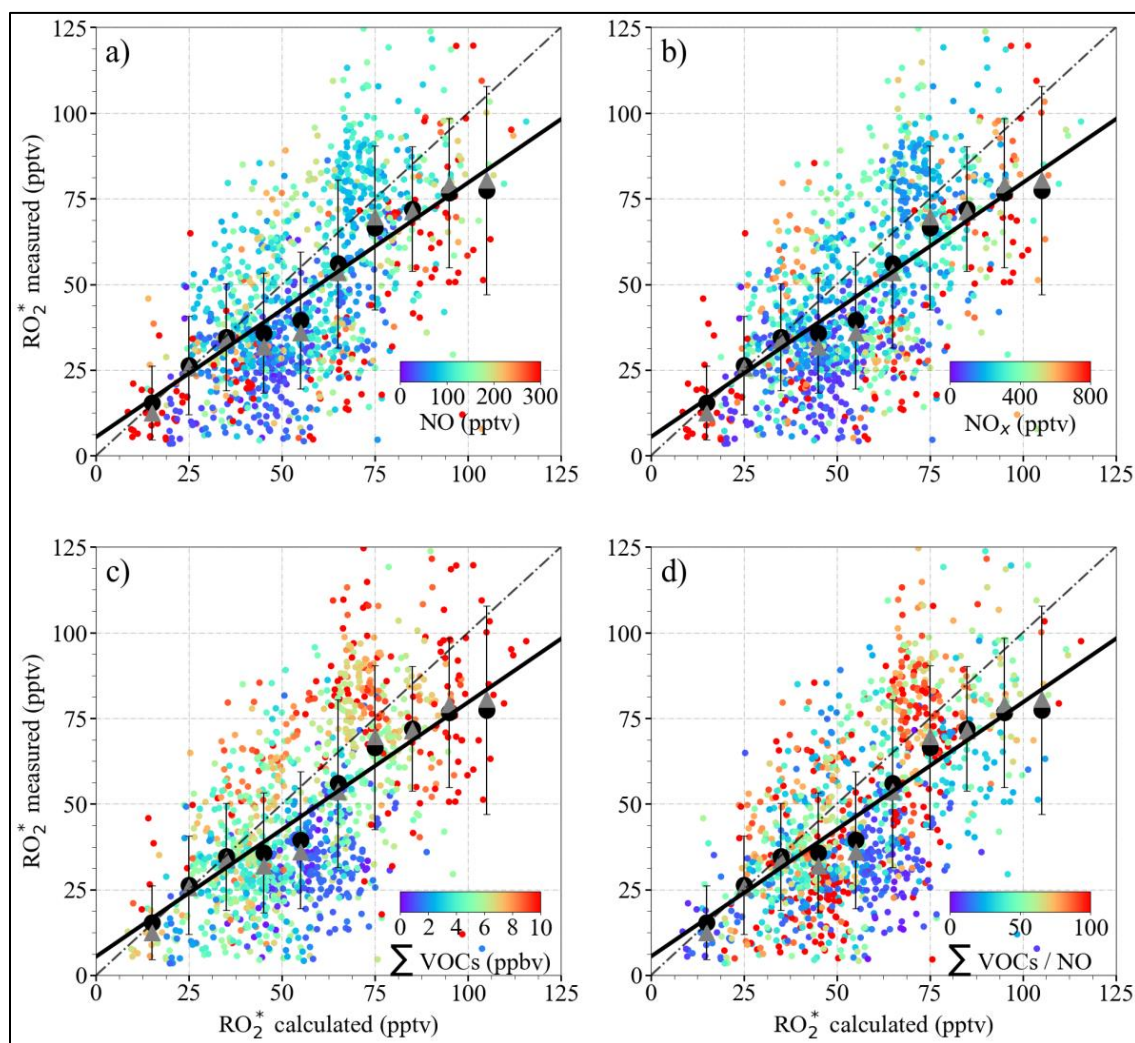
Figure 12: $RO_2{}^*_m$ versus $RO_2{}^*_c$ using Eq. 7 for $\delta = 0.5$ colour-coded with the measured a) NO mixing ratio, b) NO_x mixing ratio, c) $\Sigma VOCs$ mixing ratio, where $\Sigma VOCs = HCHO + CH_3CHO + (CHO)_2 + CH_3OH + CH_3C(O)CH_3$, and d) $\Sigma VOCs/NO$ ratio. The 1-minute (small circles), the mean of the binned $RO_2{}^*_m$ over 10 pptv $RO_2{}^*_c$ intervals (large circles), and the median of each bin (triangles) are shown. The error bars represent the $\pm 1\sigma$ standard deviation of each bin. The linear regression for the binned values (solid line) and the 1:1 relationship (dashed line) are plotted for reference.

Although considered small, the spatial and temporal differences in the in-situ measurements of the key trace gases (O_3, NO, H_2O, CO, CH_4, VOCs) as compared to those of the remote sensing observations (NO_2 and HONO) used in Eq. 7 may also contribute to the overall spread observed in Fig. 12. Although the temporal evolution and the amount of the trace gases measured using in-situ and remote sensing instruments agree reasonably well, as shown for HCHO in Fig. 13, the remote sensing instruments have, in general, larger air sampling volumes compared to that of in-situ instruments. This may occasionally lead to significant differences depending on the location of the pollutant layers with respect to HALO. In addition, PTR-MS measurements of HCHO might include interferences from molecular fragments of other compounds in the sample air (Inomata et al., 2008). Further details about the accuracy and comparability of the instrumentation on-board during the campaign can be found elsewhere (Schumann, 2020).
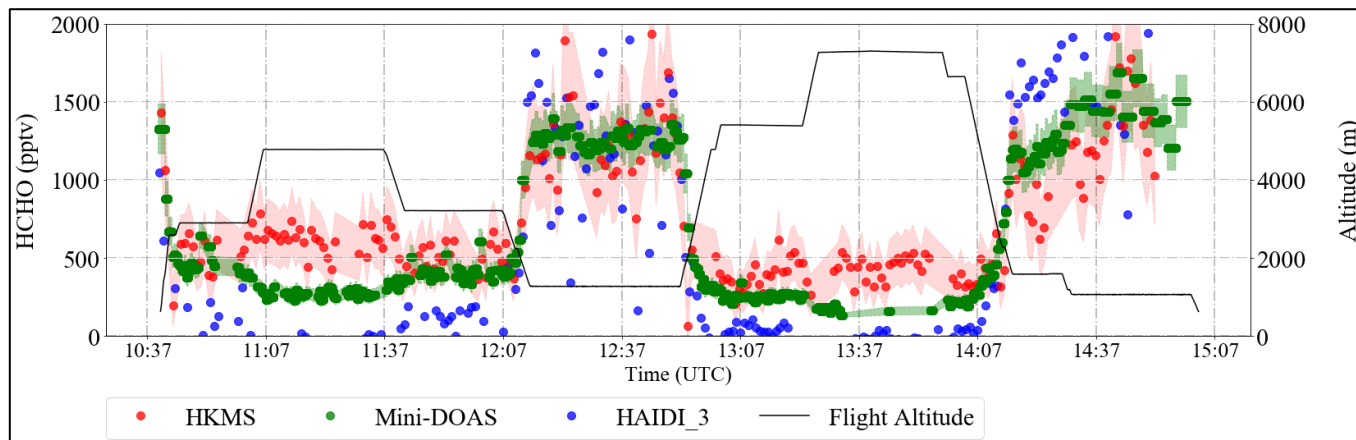
Figure 13: An example of the time series of the measured HCHO mixing ratios retrieved from the remote sensing (HAIDI in blue and miniDOAS in green) and in-situ (HKMS in red) instruments during the E-EU-04 flight on 14.07.2017. The shaded region shows $\pm 1\sigma$ uncertainties of the HKMS and miniDOAS instruments. The flight altitude is depicted in black.

In summary, apart from the inaccuracies in the reaction rate coefficients, the differences between $RO_2^*{}_m$ and $RO_2^*{}_c$ might be caused by a combined effect of the limitations of the analytical expression to simulate complex non-linear chemistry and the measurement uncertainties arising from the spatial heterogeneity of the plume for the remote sensing instruments. Consequently, the quantification of limiting factors in Eq. 7 require the analysis of the pollution events encountered along the flights individually.

The ratio of $RO_2^*{}_m$ to $RO_2^*{}_c$ ($RO_2^*{}_m/RO_2^*{}_c$) has been used to assess the applicability of Eq. 7 for the calculation of RO_2^* in the air masses probed. In Fig. 14, the data are colour-coded with respect to $RO_2^*{}_m /RO_2^*{}_c$, H_2O, ΣVOCs, and NO_x. The air masses probed at altitudes above 2000 m are close to the PSS assumptions used to develop Eq. 7, and consequently, the $RO_2^*{}_m/RO_2^*{}_c$ remains $\leq$ 1. In contrast, $RO_2^*{}_m/RO_2^*{}_c$ is at its highest value below 2000 m, reaching up to 3. At these altitudes, most of the flights in Europe were carried out in pollution plumes, in which both the amount of NO_x and RO_2^* precursors are high. The analytical expression does not capture the RO_2^* variations resulting from fast non-linear photochemistry present in these pollution plumes. This is the case for the measurements made between 42°N and 46°N in the outflow of Po Valley and Rome. ΣVOCs > 7 ppbv and NO_x mixing ratios > 500 pptv indicate high radical precursor loading and relatively fresh emissions. The $RO_2^*{}_m/RO_2^*{}_c$ is also > 2 in the measurements over the English Channel (between 50°N and 52°N) with ΣVOCs and NO_x mixing ratio > 7 ppbv and 1000 pptv, respectively.
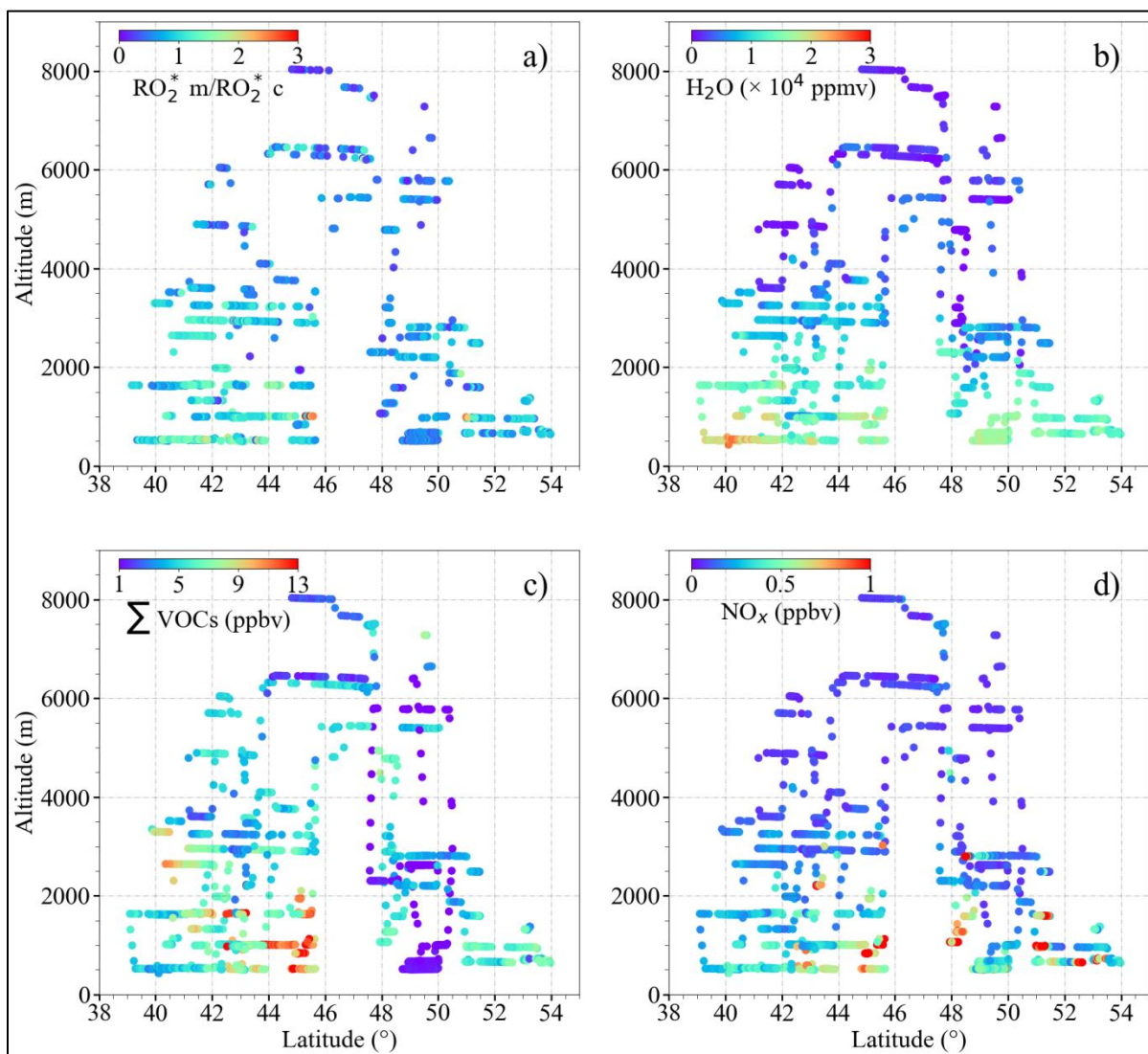
Figure 14: Plots of a) the ratio of $RO_2{}^*{}_m$ to $RO_2{}^*{}_c$ ($RO_2{}^*{}_m/RO_2{}^*{}_c$) assuming that $\delta = 0.5$; b) H_2O; c) $\sum$VOCs; d) NO_x as a function of latitude and altitude for the EMeRGe measurements in Europe.

The applicability of Eq. 7 for calculating the in-flight measurements of $RO_2{}^*$ along the track of the E-EU-03 flight on 11 July 2017 was studied in more detail. The E-EU-03 flight investigated the outflow of selected MPCs in Italy (i.e., Po Valley and Rome). Consequently, the flight track was routed along the western coast of Italy and included vertical profiling over the Tyrrhenian Sea upwind of Rome (see Fig. S6 in the supplementary information). As indicated by $j_{O(^1D)}$, in Fig. 15, cloudless conditions dominated throughout the flight track. The $RO_2{}^*{}_c$ agree reasonably well with $RO_2{}^*{}_m$ throughout this period except in the pollution plume measured from 12:05 to 12:25 UTC. In this plume, CO, NO, NO_2, HONO, NO_y, and HCHO were 100 ppbv, 180 pptv, 150 pptv, 120 pptv, 1ppbv and 2 ppbv, respectively. The $RO_2{}^*{}_m$ are approximately 20 % underestimated by $RO_2{}^*{}_c$ during this period. Backward trajectories calculated using FLEXTRA indicate the transport of pollution through the Mediterranean mixed with dust plumes originating from Tunisia. The NO mixing ratios observed indicate the proximity to emission sources.

The measurements of VOCs used in Eq. 7 may not be representative of the actual complex VOC composition in the plume measured from 12:05 to 12:25 UTC. Consequently, the RO_2 to HO_2 ratio, the branching ratios and effective rate coefficients for $RO_2{}^* - RO_2{}^*$ reactions might not be well represented in Eq. 7. Taking CH_3O_2 as a surrogate for all RO_2 might lead to uncertainties

in the RO_2^* calculations in the presence of OVOCs with larger organic chains. On the experimental side, changes in the HO_2 to RO_2 ratio affect the accuracy of the PeRCEAS retrieval of the total sum of radicals. As noted in section 3, in this study $RO_2^* = HO_2 + 0.65 \times RO_2$, and the eCL is determined for a 1:1 mixture of $HO_2:CH_3O_2$, i.e. $\delta = 0.5$ is used for the RO_2^* retrieval. However, the HO_2 to CH_3O_2 ratio is not expected to remain constant in all the air masses probed. For a 3:1 ratio of $HO_2:RO_2$, the $RO_2^*_m$ would decrease by 10 %. Similarly, a $HO_2:RO_2$ ratio of 1:3 would lead to an increase of 10 % in the reported $RO_2^*_m$. This uncertainty is well below the in-flight uncertainty of the PeRCEAS instrument indicated by the error bars in Fig. 14 (George et al., 2020), and cannot account for the overall underestimation. However, it might reduce the differences observed between $RO_2^*_m$ and $RO_2^*_c$ in particular cases. A complete explanation of the variability of RO_2^* in the pollution plumes measured within the campaign in Europe is beyond the scope of this analysis and requires an investigation by high-resolution chemical models.
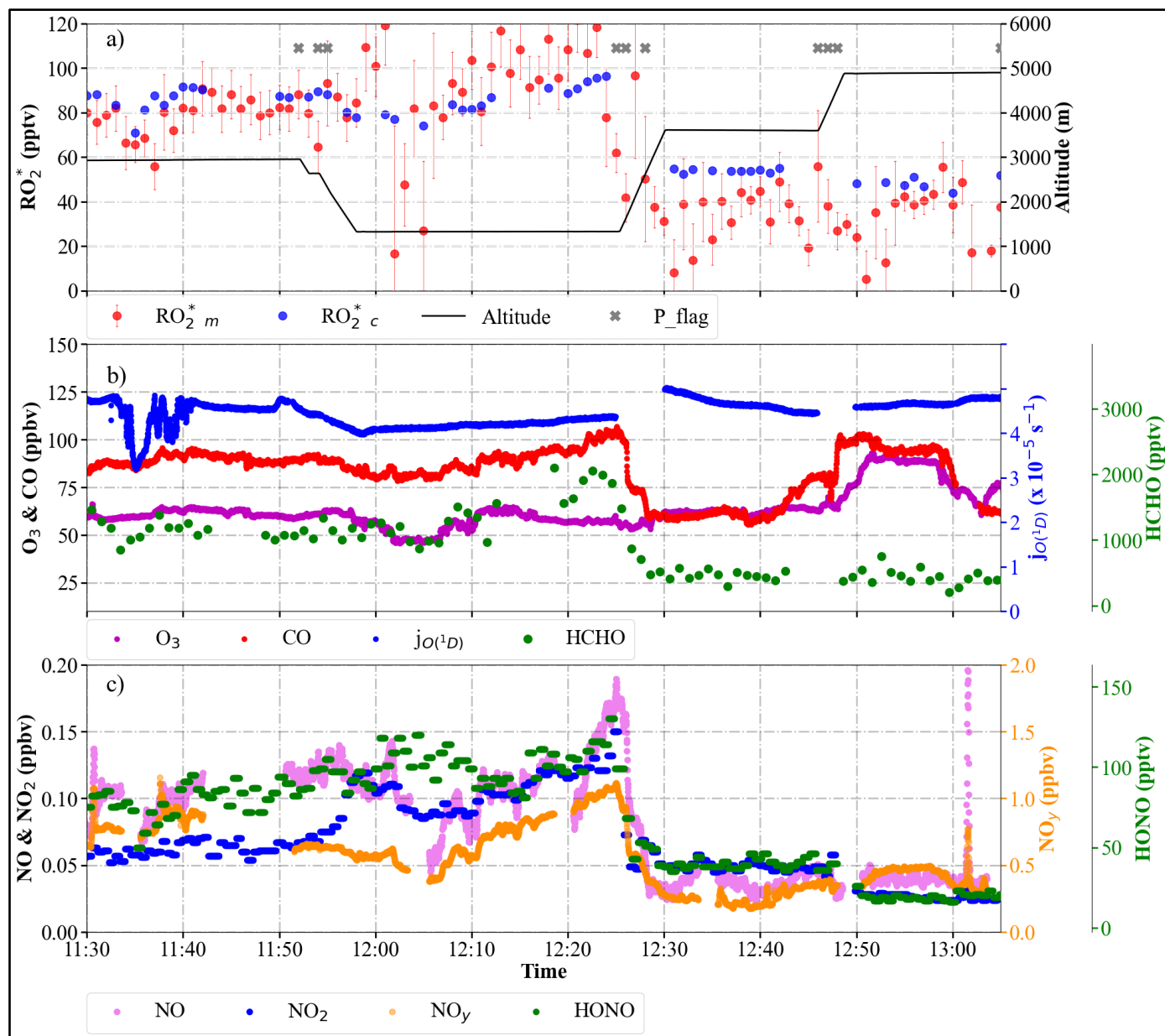
Figure 15: Temporal variation of $RO_2^*_m$ and $RO_2^*_c$, selected radical precursors and $j_{O(^1D)}$ along the E-EU-03 flight track: a) $RO_2^*_m$, $RO_2^*_c$ mixing ratios. The flight altitude is indicated in black. The P_flag indicates RO_2^* measurements affected by dynamical pressure variation in the inlet; b) O_3, CO, HCHO mixing ratios, and $j_{O(^1D)}$; c) NO, NO_2, NO_y, and HONO mixing ratios.

4.4. Comparison of results with other studies

4.4.1 RO_2^* production rate

Cantrell et al. (2003b) proposed that the production of RO_2^*, $P_{RO_2^*}$, is equal to the sum of two terms representing $RO_2^* - RO_2^*$ reactions and the $RO_2^* - NO_x$ reactions in the troposphere. As a result of this assumption, these authors describe the relationship between HO_2, RO_2, $P_{RO_2^*}$ and NO_x as:

$$P_{RO_2^*} = k_{RR} [HO_2 + RO_2]^2 + k_{RN} [HO_2 + RO_2] [NO_x] \qquad \text{(Eq. 9)}$$

where k_{RR} and k_{RN} refer to effective rate coefficients for $RO_2^* - RO_2^*$ and $RO_2^* - NO_x$ reactions, and are calculated as fit parameters. Solving Eq. 9 for $[HO_2 + RO_2]^2$ leads to:

$$[HO_2 + RO_2] = \sqrt[2]{A + B^2} - B \qquad \text{(Eq. 10)}$$

where $A = \frac{P_{RO_2^*}}{k_{RR}}$ and $B = \frac{k_{RN}[NO_x]}{2\,k_{RR}}$. For low NO_x and/or high $P_{RO_2^*}$, B becomes negligible compared to A. Then $[HO_2 + RO_2]$ approaches $\sqrt[2]{A}$ and is independent of NO_x. For high NO_x and /or low $P_{RO_2^*}$, $[HO_2 + RO_2]$ approaches zero.

The $RO_2^*{}_m$ and $RO_2^*{}_c$ for the EMeRGe observations in Europe, binned in 0.1 pptv s^{-1} $P_{RO_2^*}$ intervals, were fitted according to the procedure of Cantrel et al. (2003b) and the results are shown in Fig. 16. The obtained fit parameters for Fig. 16a and Fig. 16b are $k_{RR} = 7 \times 10^{-5}$; $k_{RN} = 9 \times 10^{-6}$. The RO_2^* calculated by Eq. 7 appears to be close to the linear function of the NO_x measured. Similar to the results of the study of Cantrell et al. (2003b), a decrease of RO_2^* with NO_x is identified for $NO_x > 1000$ pptv. $RO_2^*{}_c$ does not show the decrease with increase in NO_x for $P_{RO_2^*} \geq 0.7$ pptv s^{-1}. This might be explained by the under estimation of radical losses through organic nitrate formation in Eq. 7 as explained in section 4.3.

Despite the low agreement of the fitted lines with the $RO_2^*{}_m$, a decrease of the $RO_2^*{}_m$ as a function of NO_x is still observed. The disagreement between the $RO_2^*{}_m$ and the curves estimated using Eq. 10 implies that the simplified Eq. 9 from Cantrell et al.(2003b), is insufficient to adequately describe the chemical and physical processes occurring in the air masses probed. Part of the disagreement might arise from missing terms in the $P_{RO_2^*}$ calculated using Eq. 3 or inaccuracies related to the NO to NO_2 ratio in the air mass, which are more evident at higher $P_{RO_2^*}$. As expected, the ratio of calculated $[RO_2^*{}_c]$ to $\sqrt[2]{P_{RO_2^*}}$ has a negative linear dependence on the measured $[NO_x]$ (see Fig. 16c). The comparable relationship of $\frac{RO_2^*{}_m}{\sqrt[2]{P_{RO_2^*}}}$ to $[NO_x]$ is not linear for $NO_x < 100$ pptv approximately (see Fig. 16d). This indicates that the simplified approach of Cantrell et al. (2003b) is not applicable to the more complex non-linear processes involved in the air masses investigated within EMeRGe.
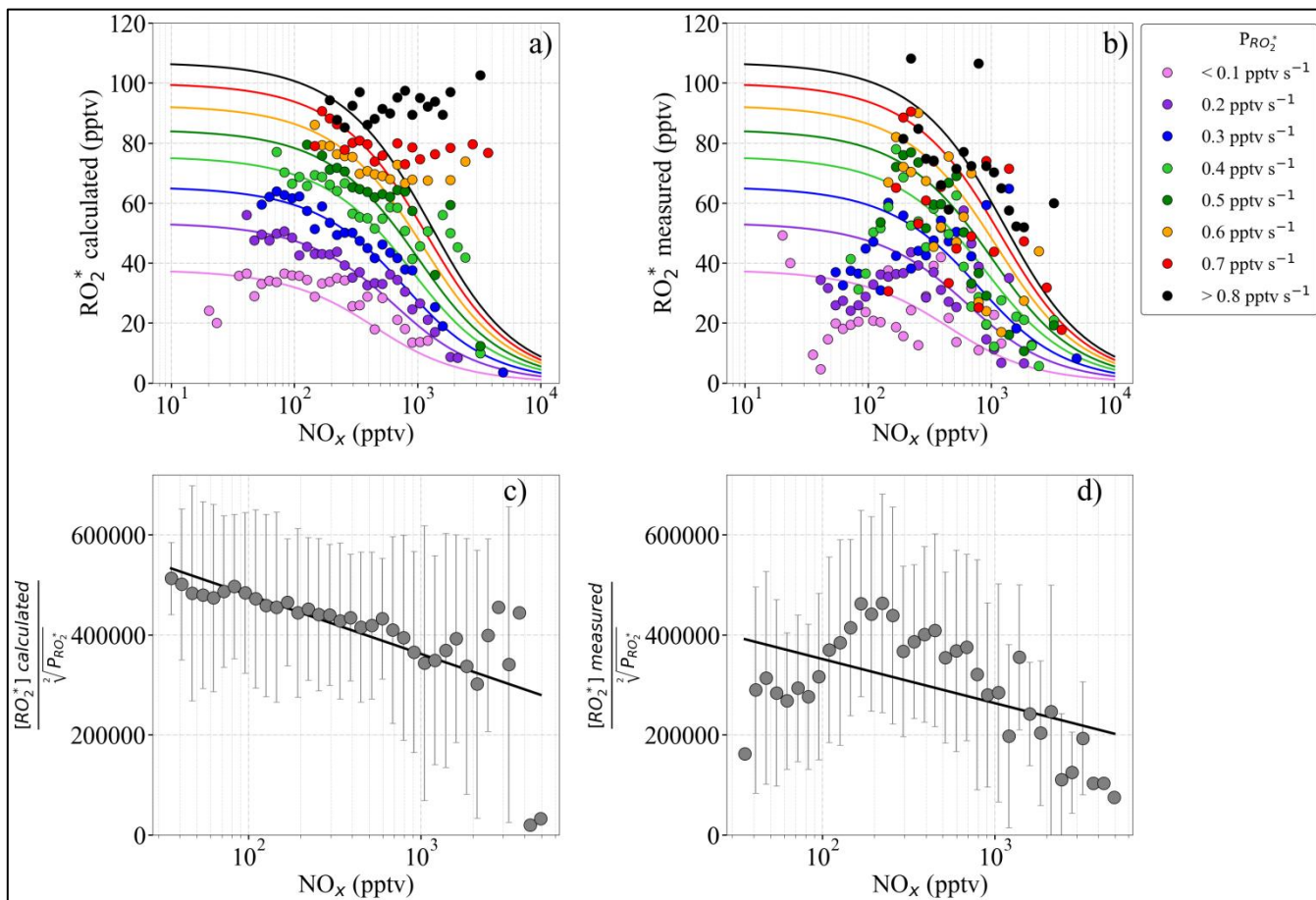
Figure 16: a) $RO_2^*{}_c$ binned into $P_{RO_2^*}$ intervals of 0.1 pptv s^{-1} versus binned NO_x ; b) $RO_2^*{}_m$ binned into $P_{RO_2^*}$ intervals of 0.1 pptv s^{-1} versus binned NO_x; c) ratio of $[RO_2^*]_c$ to $\sqrt[2]{P_{RO_2^*}}$ versus NO_x; and d) $[RO_2^*]_m$ to $\sqrt[2]{P_{RO_2^*}}$ ratio versus NO_x. The data in the a) and b) panels are assigned different colours, as a function of the radical production rate interval. The NO_x observations are binned into 560 50 equidistant intervals on a logarithmic scale. The solid lines in panels a) and b) are the least square fits, obtained using Eq. 9. In panels c) and d) the ratio of $[RO_2^*]_c$ to $\sqrt[2]{P_{RO_2^*}}$ and $[RO_2^*]_m$ to $\sqrt[2]{P_{RO_2^*}}$ are binned into 50 NOx intervals equidistant on the logarithmic scale from 10 to 10000 pptv. Error bars indicate the $\pm 1\sigma$ standard deviation for the distribution in each bin.

4.4.2 O₃ production rate

The O_3 production rate (P_{O_3}) is calculated from the EMeRGe Europe dataset using the reaction of RO_2^* with NO in a similar 565 manner to that used in previous studies of photochemical processes in urban environments (e.g. Kleinman et al., 1995; Volz-Thomas et al., 2003; Mihelcic et al., 2003; Cantrell et al., 2003b; and references herein).

$$P_{O_3} = k_{RO_2^* +NO}[RO_2^*][NO] \hspace{4cm} \text{(Eq. 11)}$$

where $k_{RO_2^*+NO}$ is taken as the average of k_{HO_2+NO} and $k_{CH_3O_2+NO}$.

Figure 17 shows the mean P_{O_3} calculated using Eq. 11 from the $RO_2^*{}_m$ and $RO_2^*{}_c$ as a function of NO. The measurements are binned 570 into 50 NO mixing ratio bins. The bin size increases with NO to keep the points equidistant on the logarithmic scale. The calculated P_{O_3} for the $RO_2^*{}_m$ and $RO_2^*{}_c$ agree well within the standard deviation of the bins.
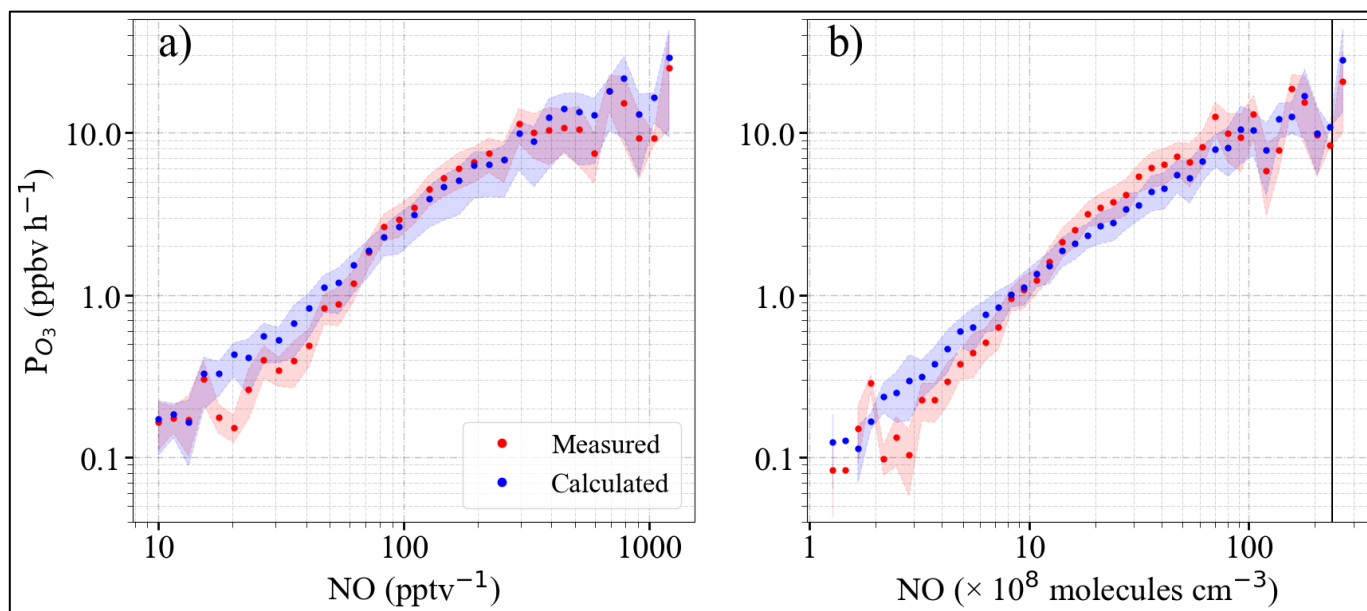
Figure 17: Calculated O_3 production rate (P_{O_3}) determined using $RO_2^*{}_m$ (red dots) and $RO_2^*{}_c$ (blue dots) as a function of: a) NO mixing ratio; b) NO number density. The 1-minute measurements are binned into 50 bins of NO equidistant on the logarithmic scale for panel a) from 10 to 10000 pptv and for panel b) from 5×10^7 to 3.5×10^{10} molecules cm⁻³ respectively. The shaded area shows the $\pm 1\sigma$ standard deviation of each bin. To facilitate comparison with ground-based measurements, the black line plotted in panel b) is the number density corresponding to 1 ppbv NO at 1000 mbar and 25°C.

Similar P_{O_3} values have been reported for ground-based measurements in polluted areas such as Wangdu (Tan et al., 2017) and Beijing (Whalley et al., 2021) and similar ranges of peroxy radicals and NO mixing ratios. In previous work, Whalley et al. (2018) calculated P_{O_3} to be about an order of magnitude lower than that found in this study from observations in central London for about an order of magnitude lower amount of $HO_2 + RO_2$. For NO > 1 ppbv, the P_{O_3} estimated from the measurement of HO_2 and RO_2, or from the assumptions of an HO_2 to RO_2 ratio were underestimated by the models in other studies in the urban atmosphere (e.g. Martinez et al., 2003; Ren et al., 2003; Kanaya et al., 2008; Mao et al., 2010; Kanaya et al., 2012; Ren et al., 2013; Brune et al., 2016; Griffith et al., 2016). This behaviour is generally attributed to an underestimate of large RO_2 concentrations, which likely undergo multiple bimolecular reactions with NO before forming an HO_2 radical.

During the EMeRGe campaign in Europe, the NO mixing ratios were < 1 ppbv (approximately < 3×10^{10} molecules cm⁻³). The ozone production rates obtained for both $RO_2^*{}_m$ and $RO_2^*{}_c$ are in reasonable agreement with other modelling studies in urban environments where the mixing ratio of NO is < 1 ppbv (Tan et al., 2017; Whalley et al., 2021)

5. Summary and conclusions

This study exploits the airborne measurements of various atmospheric constituents on-board the HALO research aircraft over Europe in summer 2017 to investigate radical photochemistry in the probed airmasses. RO_2^* are calculated by assuming a **p**hotostationary **s**teady-**s**tate (PSS) of RO_2^* and compared with the actual measurements. The calculation is constrained by the simultaneous airborne measurements of radical precursors, photolysis frequencies and reactants of RO_2^* such as NO_x and O_3. The calculated radical production rates $P_{RO_2^*}$ do not significantly vary with altitude in the air masses investigated as the increase in the photolysis frequencies as a function of altitude is concurrent with decreases in precursor concentrations.

The significance and the importance of selected initiating and terminating processes in the RO_2^* chemistry are investigated by gradually increasing the complexity of the analytical expression. The agreement of the calculations with the measurements over a wide range of chemical composition and insolation conditions improves when the analytical expression is extended to account for effective radical yields from VOC oxidation and radical losses through nitrates and nitrites formation. The RO_2^* measured is usually overestimated when NO is < 50 pptv in the air probed. This behavior might be explained by RO_2^* loss processes involving reactions with OH (e.g., the reaction of HO_2 with OH, but possibly to a lesser extent the three-body reaction of OH with itself to make H_2O_2). These reactions may become significant RO_2^* loss processes at low NO concentrations as measured during the campaign but are excluded from the analytical expression, which is constrained by on-board measurements. Similarly, the RO_2 loss through organic nitrate are also excluded from the analytical expression. These reactions may become significant RO_2^* loss processes in the presence of RO_2 with higher organic groups. This might explain some of the RO_2^* overestimations by the analytical expression observed for NO > 200 pptv.

The RO_2^* calculated under assumption of a photostationary state mostly underestimated the RO_2^* measured in polluted plumes of urban origin at altitudes below 2000 m. Changes in the HO_2 to RO_2 ratios in different plumes can account for the disagreement in particular cases. In pollution plumes with the sum of the OVOCs measured mixing ratios being higher than 7 ppbv approximately, the underestimation of the measurements can reach up to 80 %. In these plumes, the oxidation and/or photolysis of VOCs, which were not measured, and the ozonolysis of alkenes might be significant sources of RO_2^*, limiting the accuracy of the analytical expression. More information about peroxy radical speciation and VOC partitioning is required to better describe the fast photochemistry in these pollution plumes.

However, the analytical expression developed is robust enough to simulate the radical chemistry in most of the conditions in the free troposphere encountered during EMeRGe in Europe. Speciated radical and VOC measurements in future campaigns would facilitate the estimation of radical loss reactions in air masses having NO < 50 pptv and improve radical production rates estimations in pollution plumes having a high amount of VOCs, where non-linear complex chemistry is involved. Comparing RO_2^* measurements with RO_2^* calculations from the analytical expression helps to identify different chemical and physical regimes, which can be used to constrain future model studies.

The calculated O_3 production rates for NO < 1 ppbv are in the same order of magnitude as those previously reported for urban environments. This indicates that the selected RO_2^* production and loss processes and observations of the radical precursors on-board are, to a good approximation, adequate for the estimation of the O_3 production in the measured airmasses in the free troposphere over Europe.

Disclaimer. Competing interests. The authors declare that they have no conflict of interest.

Disclaimer. Financial support. The study was funded in part by the German Research Foundation (Deutsche Forschungsgemeinschaft; DFG) HALO-SPP 1294, the University and the State of Bremen, IPA, DLR, Oberpfaffenhofen, Germany. The contributions from BS, FK, and KP were supported via the DFG grants PF 384/16, PF 384/17 and PF 384/19. KB was granted funding via the DFG grant Pl 193/21-1 and acknowledges additional financial from the Heidelberg Graduate School for Physics. EF was supported via the DFG grant NE 2150/1-1 and acknowledges additional financial support from the Karlsruhe Institute of Technology. MG, YL, MDAH and JPB acknowledge financial support from the University of Bremen.

Acknowledgements

Author contribution:

MG, VN, and YL undertook the RO_2^* measurements, flying as key scientists on-board HALO. VN led the deployment of PeRCEAS in the HALO aircraft. MG led the analysis of the PeCEAS measurements and prepared the manuscript with contributions from all co-authors. MDAH and JPB initiated the EMeRGe research project and consortium, acted as co-principal and principal investigators, and participated in the measurement campaigns. They developed the overarching EMeRGe scientific objectives and the required measurement portfolio, directed the EMeRGe research campaigns, and participated in the data analysis presented. AZ, BB, BS, EF, FO, FK, HS, HZ, KB, KP, and TH have contributed by providing their measurements made on-board HALO during the campaign and participated in the discussion of results.

Competing interests:

The authors declare that they have no conflict of interest.

6. References

Andreae, M. O. , Afchine, A. Albrecht, R., Holanda, B. A., Artaxo, P., Barbosa, H. M. J., Borrmann, S., Cecchini, M. A., Costa, A., Dollner, M., Fütterer, D., Järvinen, E., Jurkat, T., Klimach, T., Konemann, T., Knote, C., Krämer, M., Krisna, T., Machado, L. A. T., Mertes, S.; Minikin, A. , Pöhlker, C., Pöhlker, M. L., Pöschl, U. Rosenfeld, D., Sauer, D., Schlager, H., Schnaiter, M., Schneider, J., Schulz, C., Spanu, A., Sperling, V. B., Voigt, C., Walser, A., Wang, J., Weinzierl, B., Wendisch, M. , Ziereis, H.: Aerosol characteristics and particle production in the upper troposphere over the Amazon Basin. Atmos. Chem. Phys., 18, 921–961, https://doi.org/ 10.5194/acp-18-921-2018, 2018.

Andrés-Hernández, M. D., Kartal, D., Reichert, L., Burrows, J. P., Meyer Arnek, J., Lichtenstern, M., Stock, P., and Schlager, H.: Peroxy radical observations over West Africa during AMMA 2006: photochemical activity in the outflow of convective systems, Atmos. Chem. Phys., 9, 3681–3695, https://doi.org/10.5194/acp-9-3681-2009, 2009.

Andrés Hernández, M. D., Hilboll, A., Ziereis, H., Förster, E., Krüger, O. O., Kaiser, K., Schneider, J., Barnaba, F., Vrekoussis, M., Schmidt, J., Huntrieser, H., Blechschmidt, A.-M., George, M., Nenakhov, V., Klausner, T., Holanda, B. A., Wolf, J., Eirenschmalz, L., Krebsbach, M., Pöhlker, M. L., Hedegaard, A. B., Mei, L., Pfeilsticker, K., Liu, Y., Koppmann, R., Schlager, H., Bohn, B., Schumann, U., Richter, A., Schreiner, B., Sauer, D., Baumann, R., Mertens, M., Jöckel, P., Kilian, M., Stratmann, G., Pöhlker, C., Campanelli, M., Pandolfi, M., Sicard, M., Gomez-Amo, J. L., Pujadas, M., Bigge, K., Kluge, F., Schwarz, A., Daskalakis, N., Walter, D., Zahn, A., Pöschl, U., Bönisch, H., Borrmann, S., Platt, U., and Burrows, J. P.: Overview: On the transport and transformation of pollutants in the outflow of major population centres – observational data from the EMeRGe European intensive operational period in summer 2017, Atmos. Chem. Phys., 22, 5877–5924, 2022 https://doi.org/10.5194/acp-22-5877-2022, 2022 Brito, J., and Zahn, A.: An unheated permeation device for calibrating atmospheric VOC measurements, Atmos. Meas. Tech., 4(10), 2143–2152, https://doi.org/ 10.5194/amt-4-2143-2011, 2011.

Brune, W. H., Baier, B. C., Thomas, J., Ren, X., Cohen, R. C., Pusede, S. E., Browne, E. C., Goldstein, A. H., Gentner, D. R., Keutsch, F. N., Thornton, J. A., Harrold, S., Lopez-Hilfiker, F. D., and Wennberg, P. O.: Ozone production chemistry in the presence of urban plumes, Faraday Discuss., 189, 169–189, https://doi.org/10.1039/c5fd00204d, 2016.

Burkholder, J. B., Sander, S. P., Abbatt, J., Barker, J. R., Huie, R. E., Kolb, C. E., Kurylo, M. J., Orkin, V. L. Wilmouth, D. M., and Wine P. H.: Chemical Kinetics and Photochemical Data for Use in Atmospheric Studies, Evaluation No. 18, JPL Publication 15-10, Jet Propulsion Laboratory, Pasadena, available at: http: //jpldataeval.jpl.nasa.gov (last access: 7 April 2020), 2015.

Cantrell, C. A. and Stedman, D. H.: A possible technique for the measurement of atmospheric peroxy radicals, Geophys. Res. Lett., 9, 846–849, 1982.

Cantrell, C. A., Stedman, D. H., and Wendel, G. J.: Measurement of atmospheric peroxy radicals by chemical amplification, Anal. Chem., 56, 1496–1502, 1984

Cantrell, C. A., Shetter, R. E., Calvert, J. G., Eisele, F. L., Williams, E., Baumann, K., Brune, W. H., Stevens, P. S., Mather J. H.: Peroxy radicals from photostationary state deviations and steady state calculations during the Tropospheric OH Photochemistry Experiment at Idaho Hill, Colorado, 1993, J. Geophys. Res., 102(D5), 6369, https://doi.org/ https://doi.org/10.1029/96JD01703, 1997.

Cantrell, C. A., G. D. Edwards, S. Stephens, L. Mauldin, E. Kosciuch, M. Zondlo, and F. Eisele.: Peroxy radical observations using chemical ionisation mass spectrometry during TOPSE, J. Geophys. Res., 108(D6), 8381, https://doi.org/10.1029/2002JD002715, 2003a.

Cantrell, C. A., Edwards, G. D., Stephens, S., Mauldin, R.L., Zondlo. M.A., Kosciuch, E., Eisele, F. L., Shetter, R. E., Lefer, B. L., Hall, S., Flocke, F., Weinheimer, A., Fried, A., Apel, E., Kondo, Y., Blake, D. R., Blake, N. J., Simpson, I. J., Bandy, A. R., Thornton, D. C., Heikes, B. G., Singh, H. B., Brune, W. H., Harder, H., Martinez, M., Jacob, D. J., Avery, M. A., Barrick, J. D., Sachse, G. W., Olson, J. R., Crawford, J. H., and Clarke, A. D.: Peroxy radical behaviour during the Transport and Chemical Evolution over the Pacific (TRACE-P) campaign as measured aboard the NASA -3B aircraft, J. Geophys. Res., 108(D20), 8797, https://doi.org/10.1029/2003JD003674, 2003b.

Chen H., Winderlich, J., Gerbig, C., Hoefer, A., Rella, C. W., Crosson, E. R., Van Pelt, A. D., Steinbach, J., Kolle, O., Beck, V., Daube, B. C., Gottlieb, E. W., Chow, V. Y., Santoni, G. W., and S. C. Wofsy, High-accuracy continuous airborne measurements of greenhouse gases (CO2 and CH4) using the cavity ring-down spectroscopy (CRDS) technique, Atmos. Mes. Tech., 3, 375-386, 2010.

Crawford, J., Davis, D., Olson, J., Chen, G., Liu, S., Gregory, G., Barrick, J., Sachse, G., Sandholm, S., Heikes, B., Singh, H., and Blake, D.: Assessment of upper tropospheric HOx sources over the tropical Pacific based on NASA GTE/PEM data: Net effect on HOx and other photochemical parameters, J. Geophys. Res., 104, 16255–16273, https://doi.org/10.1029/1999JD900106, 1999.

Fisher, R., Lowry, D., Wilkin, O., Sriskantharajah, S., and Nisbet, E. G.: High-precision, automated stable isotope analysis of atmospheric methane and carbon dioxide using continuous-flow isotope-ratio mass spectrometry, Rapid communications in mass spectrometry: RCM, 20 (2), 200–208. https://doi.org/10.1002/rcm.2300, 2006.

Fricke, C., Ehrlich, A., Jäkel, E., Bohn, B., Wirth, M., and Wendisch, M.: Influence of local surface albedo variability and ice crystal shape on passive remote sensing of thin cirrus, Atmos. Chem. Phys.,14, 1943-1958, https://doi.org/10.5194/acp-14-1943-2014, 2014.

General, S., Pöhler, D., Sihler, H., Bobrowski, N., Frieß, U., Zielcke, J., Horbanski, M., Shepson, P. B., Stirm, B. H., Simpson, W. R., Weber, K., Fischer, C., and Platt, U.: The Heidelberg Airborne Imaging DOAS Instrument (HAIDI) – a novel Imaging DOAS device for 2-D and 3-D imaging of trace gases and aerosols, Atmos. Meas. Tech., 7, 3459-3485, 2014, https://doi.org/10.5194/amt-7-3459-2014.

George, M., Andrés-Hernández, M. D., Nenakhov, V., Liu, Y., and Burrows, J. P.: Airborne measurement of peroxy radicals using chemical amplification coupled with cavity ring-down spectroscopy: the PeRCEAS instrument, Atmos. Meas. Tech 13, 2577–2600, https://doi.org/ 10.5194/amt-13-2577-2020.

George, M. Phd thesis, Airborne measurement and interpretation of peroxy radical concentrations with a focus on the oxidation mechanisms in the Asian free troposphere, PhD therisi, Universtity of Bremen 2022

Gerbig, C., Kley, D., Volz-Thomas, A., Kent, J., Dewey, K., and McKenna, D. S.: Fast response resonance fluorescence CO measurements aboard the C-130: Instrument characterisation and measurements made during North Atlantic Regional Experiment 1993, J. Geophys. Res., 101, 29229-29238, 1996.

Griffith, S. M., Hansen, R. F., Dusanter, S., Michoud, V., Gilman, J. B., Kuster, W. C., Veres, P. R., Graus, M., de Gouw, J. A., Roberts, J., Young, C., Washenfelder, R., Brown, S. S., Thalman, R., Waxman, E., Volkamer, R., Tsai, C., Stutz, J., Flynn, J. H., Grossberg, N., Lefer, B., Alvarez, S. L., Rappenglueck, B., Mielke, L. H., Osthoff, H. D., and Stevens, P. S.: Measurements of Hydroxyl and Hydroperoxy Radicals during CalNexLA: Model Comparisons and Radical Budgets, J. Geophys. Res.-Atmos., 121, 4211–4232, https://doi.org/10.1002/2015JD024358, 2016.

Horstjann, M., Andrés Hernández, M. D., Nenakhov, V., Chrobry, A., and Burrows, J. P.: Peroxy radical detection for airborne atmospheric measurements using absorption spectroscopy of NO_2, Atmos. Meas. Tech. 7, 1245-1257, https://doi.org/ 10.5194/amt-7-1245-2014.

Hüneke, T., Aderhold, O.-A., Bounin, J., Dorf, M., Gentry, E., Grossmann, K., Grooß, J.-U., Hoor, P., Jöckel, P., Kenntner, M., Knapp, M., Knecht, M., Lörks, D., Ludmann, S., Matthes, S., Raecke, R., Reichert, M., Weimar, J., Werner, B., Zahn, A., Ziereis, H., and Pfeilsticker, K.: The novel HALO mini-DOAS instrument: inferring trace gas concentrations from airborne UV/visible limb spectroscopy under all skies using the scaling method, Atmos. Meas. Tech., 10, 4209–4234, https://doi.org/10.5194/amt-10-4209-2017, 2017.

Inomata, S., Tanimoto, H., Kameyama, S., Tsunogai, U., Irie, H., Kanaya, Y., and Wang, Z.: Technical Note: Determination of formaldehyde mixing ratios in air with PTR-MS: laboratory experiments and field measurements, Atmos. Chem. Phys., 8, 273–284, https://doi.org/10.5194/acp-8-273-2008, 2008.

Kanaya, Y., Fukuda, M., Akimoto, H., Takegawa, N., Komazaki, Y., Yokouchi, Y., Koike, M., and Kondo, Y.: Urban photochemistry in central Tokyo: 2. Rates and regimes of oxidant (O3 + NO2) production, J. Geophys. Res., 113, D06301, https://doi.org/10.1029/2007JD008671, 2008.

Kanaya, Y., Hofzumahaus, A., Dorn, H.-P., Brauers, T., Fuchs, H., Holland, F., Rohrer, F., Bohn, B., Tillmann, R., Wegener, R., Wahner, A., Kajii, Y., Miyamoto, K., Nishida, S., Watanabe, K., Yoshino, A., Kubistin, D., Martinez, M., Rudolf, M., Harder, H., Berresheim, H., Elste, T., Plass-Dülmer, C., Stange, G., Kleffmann, J., Elshorbany, Y., and Schurath, U.: Comparisons of observed

and modeled OH and HO2 concentrations during the ambient measurement period of the HOxComp field campaign, Atmos. Chem. Phys., 12, 2567–2585, https://doi.org/10.5194/acp-12-2567-2012, 2012.

735   Kartal, D., Andrés-Hernández, M. D., Reichert, L., Schlager, H., and Burrows, J. P.: Technical Note: Characterisation of a DUALER instrument for the airborne measurement of peroxy radicals during AMMA 2006, Atmos. Chem. Phys., 10, 3047–3062, https://doi.org/10.5194/acp-10-3047-2010, 2010.

Kleinman, L., Y.-N. Lee, S. R. Springston, J. H. Lee, L. Nunnermacker, J. Weinstein-Lloyd, X. Zhou, and L. Newman, Peroxy radical concentration and ozone formation rate at a rural site in southeastern United States, J. Geophys. Res., 100, 7263– 7273,
740   1995.

Kluge, F., Hüneke, T., Knecht, M., Lichtenstern, M., Rotermund, M., Schlager, H., Schreiner, B., and Pfeilsticker, K.: Profiling of formaldehyde, glyoxal, methylglyoxal, and CO over the Amazon: normalized excess mixing ratios and related emission factors in biomass burning plumes, Atmos. Chem. Phys., 20, 12363–12389, https://doi.org/10.5194/acp-20-12363-2020, 2020.

Lew, M. M., Rickly, P. S., Bottorff, B. P., Reidy, E., Sklaveniti, S., Léonardis, T., Locoge, N., Dusanter, S., Kundu, S., Wood, E.,
745   and Stevens, P. S.: OH and HO2 radical chemistry in a midlatitude forest: measurements and model comparisons, Atmos. Chem. Phys., 20, 9209–9230, https://doi.org/10.5194/acp-20-9209-2020, 2020.

Mallaun, C., Giez, A. and Baumann, R.: Calibration of 3-D wind measurements on a single engine research aircraft Atmos. Meas. Tech., 8, 3177-3196, https://doi.org/ 10.5194/amt-8-3177-2015, 2015.

Mao, J., Jacob, D. J., Evans, M. J., Olson, J. R., Ren, X., Brune, W. H., Clair, J. M. St., Crounse, J. D., Spencer, K. M., Beaver,
750   M. R., Wennberg, P. O., Cubison, M. J., Jimenez, J. L., Fried, A., Weibring, P., Walega, J. G., Hall, S. R., Weinheimer, A. J., Cohen, R. C., Chen, G., Crawford, J. H., McNaughton, C., Clarke, A. D., Jaeglé, L., Fisher, J. A., Yantosca, R. M., Le Sager, P., and Carouge, C.: Chemistry of hydrogen oxide radicals (HOx) in the Arctic troposphere in spring, Atmos. Chem. Phys., 10, 5823– 5838, https://doi.org/10.5194/acp-10-5823-2010, 2010.

Parrish, D. D., Trainer, M., Williams, E. J., Fahey, D. W., Hobler, G., Eubank, C. S., Liu, S.C., Murphy, P. C. , Albritton, D. L.
755   and Fehsenfeld, F. C.: Measurements of the NOx-O3 photostationary state at Niwot Ridge, Colorado, J. Geophys. Res., 91, No.D5, 5361 – 5370, 1986.

Ren, X., Harder, H., Martinez, M., Lesher, R. L., Oliger, A., Shirley, T., Adams, J., Simpas, J. B., and Brune, W. H.: HOX concentrations and OH reactivity observations in New York City during PMTACS-NY2001, Atmos. Environ., 37, 3627–3637, 2003.

760   Ren, X., van Duin, D., Cazorla, M., Chen, S., Mao, J., Zhang, L., Brune, W. H., Flynn, J. H., Grossberg, N., Lefer, B. L., Rappenglück, B., Wong, K. W., Tsai, C., Stutz, J., Dibb, J. E., Thomas Jobson, B., Luke, W. T., and Kelley, P.: Atmospheric oxidation chemistry and ozone production: Results from SHARP 2009 in Houston, Texas, J. Geophys. Res., 118, 5770–5780, https://doi.org/10.1002/jgrd.50342, 2013.

Ren, Y., Baumann, R., Schlager, H.: An airborne perfluorocarbon tracer system and its first application for a Lagrangian
765   experiment. Atmos. Meas. Tech., 8, 69-80. https://doi.org/ 10.5194/ amt-8-69-2015, 2015.

Ridley, B.A., Madronich, S., Chatfield, R. B., Walega, J. G., and Shetter, R. E.: Measurements and model simulations of the photostationary state during the Mauna Loa observatory photochemistry experiment: Implications for radical concentrations and ozone production and loss rates, J. Geophys. Res. 97, 10375-10388 (1992).

770 Rotermund, M. K., Bense, V., Chipperfield, M. P., Engel, A., Grooß, J.-U., Hoor, P., Hüneke, T., Keber, T., Kluge, F., Schreiner, B., Schuck, T., Vogel, B., Zahn, A., and Pfeilsticker, K.: Organic and inorganic bromine measurements around the extratropical tropopause and lowermost stratosphere: Insights into the transport pathways and total bromine, Atmos. Chem. Phys. Discuss. [preprint], https://doi.org/10.5194/acp-2021-202, in review, 2021.

Stutz, J., Werner, B., Spolaor, M., Scalone, L., Festa, J., Tsai, C., Cheung, R., Colosimo, S. F., Tricoli, U., Raecke, R., Hossaini, R., Chipper1180 field, M. P., Feng, W., Gao, R.-S., Hintsa, E. J., Elkins, J. W., Moore, F. L., Daube, B., Pittman, J., Wofsy, S., 775 and Pfeilsticker, K.: A new Differential Optical Absorption Spectroscopy instrument to study atmospheric chemistry from a high-altitude unmanned aircraft, Atmos. Meas. Tech., 10, 1017 – 1042, https://doi.org/10.5194/amt-10-1017-2017, 2017.

Schulz, C., Schneider, J., Holanda, B. A., Appel, O., Costa, A., de Sá, S.S., Dreiling, V. Fütterer, D., Jurkat-Witschas, T., Klimach, T., Knote, C., Krämer, M., Martin, S.T., Mertes, S., Pöhlker, M.L., Sauer, D., Voigt, C., Walser, A., Weinzierl, A.B., Ziereis, H., Zöger, M., Andreae, M.O., Artaxo, P., Machado, L-A.T., Pöschl, U., Wendisch, M., and S. Borrmann, Aircraft-based observations 780 of isoprene-epoxydiol-derived secondary organic aerosol (IEPOX-SOA) in the tropical upper troposphere over the Amazon region. Atmos. Chem. Phys., 18, 14979–15001, 2018, https://doi.org/ 10.5194/acp-18-14979-2018.

Schumann, U.: Measurement and model data comparisons for the HALO-FAAM formation flight during EMeRGe on 17 July 2017, doi.:10.5281/zenodo.4427965, 2020.

Speidel, M., Nau, R., Arnold, F., Schlager, H., A. Stohl, Sulfur dioxide measurements in the lower, middle and upper troposphere: 785 Deployment of an aircraft-based chemical ionisation mass spectrometer with permanent in-flight calibration, Atmospheric Environment, 41, 2427-2437, https://doi.org/10.1016/j.atmosenv. 2006.07.047. 2007.

Tan, D., Faloona, I., Simpas, J. B., Brune, W., Olson, J., Crawford, J., Avery, M., Sachse, G., Vay, S., Sandholm, S., Guan, H.-W., Vaughn, T., Mastromarino, J., Heikes, B., Snow, J., Podolske, J., and Singh, H.: OH and HO2 in the tropical Pacific: Results from PEMTropics B, J. Geophys. Res., 106, 32,667–32,681, 2001.

790 Tan, Z., Fuchs, H., Lu, K., Hofzumahaus, A., Bohn, B., Broch, S., Dong, H., Gomm, S., Häseler, R., He, L., Holland, F., Li, X., Liu, Y., Lu, S., Rohrer, F., Shao, M., Wang, B., Wang, M., Wu, Y., Zeng, L., Zhang, Y., Wahner, A., and Zhang, Y.: Radical chemistry at a rural site (Wangdu) in the North China Plain: observation and model calculations of OH, HO2 and RO2 radicals, Atmos. Chem. Phys., 17, 663–690, https://doi.org/10.5194/acp-17-663-2017, 2017.

Tyndall, G. S.; Cox, R. A.; Granier, C.; Lesclaux, R.; Moortgat, G. K.; Pilling, M. J.; Ravishankara, A. R.; Wallington, T. J. 795 Atmospheric chemistry of small organic peroxy radicals. J. Geophys. Res. 2001, 106, 12157-12182, https://doi.org/10.1029/2000JD900746.

Volz-Thomas, A., Xueref, I., and Schmitt, R.: Automatic gas chromatograph and calibration system for ambient measurements of PAN and PPN, Environ. Sci. Poll. Res., 9, 72-76, 2001.

Volz-Thomas, A., Pätz, H‑W., Houben, N., Konrad, S., Mihelcic, D., Klüpfel, T.. Perner, D.: Inorganic trace gases and peroxy radicals during BERLIOZ at Pabstthum: An investigation of the photostationary state of NO_x and O_3, J. Geophys. Res., 108(D4), PHO 4-1, https://doi.org/ https://doi.org/10.1029/2001JD001255, 2003.

Wendisch, M., Pöschl, U., Andreae, M. O., Machado, L. A. T., Albrecht, R., Schlager, H., Rosenfeld, D., Martin, S. T., Abdelmonem, A. Afchine, A., Araùjo, A. C., Artaxo, P., Aufmhoff, H. Barbosa, H. M. J., Borrmann, S., Braga, R., Buchholz, B., Cecchini, M. A., Costa, A. Curtius, J., Dollner, M., Dorf, M., Dreiling, V., Ebert, V., Ehrlich, A., Ewald, F., Fisch, G., Fix, A., Frank, F., Fütterer, D., Heckl, C., Heidelberg, F., Hüneke, T., Jäkel, E., Järvinen, E., Jurkat, T., Kanter, S., Kästner, U., Kenntner, M., Kesselmeier, J., Klimach, T., Knecht, M., Kohl, R., Kölling, T., Krämer, M., Krüger, M., Krisna, T. C., Lavric, J. V., Longo, K., Mahnke, C., Manzi, A. O., Mayer, B., Mertes, S., Minikin, A., Molleker, S., Münch, S., Nillius, B., Pfeilsticker, K., Pöhlker, C., Roiger, A., Rose, D., Rosenow, D., Sauer, D., Schnaiter, M., Schneider, J., Schulz, C., de Souza, R. A. F. Spanu, A., Stock, P., Vila, D., Voigt, C., Walser, A., Walter, D., Weigel, R., Weinzierl, B., Werner, F., Yamasoe, M. A., Ziereis, H., Zinner, T., and Zöger, M.: The ACRIDICON-CHUVA campaign: Studying tropical deep convective clouds and precipitation over Amazonia using the new German research aircraft HALO, Bull. Amer. Meteorol. Soc., 97, 1885-1908, https://doi.org/ 10.1175/BAMS-D-14-00255, 2016.

Whalley, L. K., Slater, E. J., Woodward-Massey, R., Ye, C., Lee, J. D., Squires, F., Hopkins, J. R., Dunmore, R. E., Shaw, M., Hamilton, J. F., Lewis, A. C., Mehra, A., Worrall, S. D., Bacak, A., Bannan, T. J., Coe, H., Percival, C. J., Ouyang, B., Jones, R. L., Crilley, L. R., Kramer, L. J., Bloss, W. J., Vu, T., Kotthaus, S., Grimmond, S., Sun, Y., Xu, W., Yue, S., Ren, L., Acton, W. J. F., Hewitt, C. N., Wang, X., Fu, P., and Heard, D. E.: Evaluating the sensitivity of radical chemistry and ozone formation to ambient VOCs and NOx in Beijing, Atmos. Chem. Phys., 21, 2125–2147, https://doi.org/10.5194/acp-21-2125-2021, 2021.

Wintel, J., Hösen, E., Koppmann, R., Krebsbach, M., Hofzumahaus, A., and Rohrer, F.: Stable carbon isotope ratios of toluene in the boundary layer and the lower free troposphere, Atmos. Chem. Phys., 13, 11059-11071, https://doi.org/10.5194/acp-13-11059-2013, 2013.

Zahn, A., Weppner, J., Widmann, H., Schlote-Holubek, K., Burger, B., Kühner, T., Franke, H.: A fast and precise chemiluminescence ozone detector for eddy flux and airborne application, Atmos. Meas. Tech., 5 (2), 363–375. https://doi.org/10.5194/amt-5-363-2012, 2012.

Zarzana, K. J., Min, K.-E., Washenfelder, R. A., Kaiser, J., Krawiec-Thayer, M., Peischl, J., Neuman, J. A., Nowak, J. B., Wagner, N. L., Dubè, W. P., St. Clair, J. M., Wolfe, G. M., Hanisco, T. F., Keutsch, F. N., Ryerson, T. B., and Brown, S. S.: Emissions of Glyoxal and Other Carbonyl Compounds from Agricultural Biomass Burning Plumes Sampled by Aircraft, Environ. Sci. Technol., 51, 11761–11770, https://doi.org/10.1021/acs.est.7b03517, 2017.

Ziereis, H., Minikin, A., Schlager, H., Gayet, J.F., Auriol, F., Stock, P., Baehr, J., Petzold, A., Schumann, U., Weinheimer, A., Ridley, B., and Ström, J.: Uptake of reactive nitrogen on cirrus cloud particles during INCA, Geophys. Res. Lett., 31(5), 2004.